Favorable trade-off between heat transfer and pressure drop in 3D printed baffled logpile catalyst structures

Available online at www.sciencedirect.com

Chemical Engineering Research and Design

journal homepage: www.elsevier.com/locate/cherd

Favorable trade-off between heat transfer and pressure drop in 3D printed baffled logpile catalyst structures

Leon R.S. Rosseau, Jord T.A. Jansen, Ivo Roghair, Martin van Sint Annaland *

Department of Chemical Engineering and Chemistry, Eindhoven University of Technology, P.O. Box 513, Eindhoven 5600MB, the Netherlands

ARTICLE INFO

Article history:
Received 6 February 2023
Received in revised form 10 May 2023
Accepted 21 June 2023
Available online 24 June 2023

Keywords:
Heat transfer
Pressure drop
Additive manufacturing
Baffles
Process intensification
Computational Fluid Dynamics

ABSTRACT

Additive manufacturing has the potential to unlock a large degree of geometric freedom in the shaping of catalytic material, thereby providing new possibilities to optimize catalyst holdup, pressure drop and heat and mass transfer characteristics. In this modelling study, baffled logpile structures are proposed as a promising candidate to exploit this potential, by shaping the catalytic material as a static mixer, generating cross-flow. An OpenFOAM Computational Fluid Dynamics study was performed on various 2D structure designs to map the trade-off between heat transfer, pressure drop and residence time distribution as a function of the design, length and gap spacing of the baffle. It is observed that structures with the longest baffles provide optimal heat transfer performance, and that the baffle gap spacing can be used to tailor the trade-off between heat transfer and pressure drop. In comparison to a packed bed filled with spherical particles, the novel structures offer a heat transfer rate four to six times as high at the same pressure drop. Whilst full 3D simulations, validated by experiments, remain to complete the analysis, the current work illustrates the potential of this novel class of structured catalyst materials for intensified chemical reactors.

1. Introduction

Heterogeneous catalysis is used in a plethora of different chemical conversions (Friend and Xu, 2017). Successful application of a heterogeneous catalyst requires not only chemical, but also engineering considerations, particularly related to the shaping and packing of the material (Mitchell et al., 2013). For many processes, the catalyst powder is compressed or extruded in spherical or cylindrical geometries and randomly packed in so-called packed bed reactors (Kraushaar-Czarnetzki and Müller, 2009; Hagen, 2015). The advantage of such reactors is the high catalyst loading, but both the geometry of the individual pellet, as well as the packing structure and procedure, influence the operating characteristics and performance of the reactor and require careful attention (Afandizadeh and Foumeny, 2001; Allen et al., 2013; Ravindran and Madhu, 2020). The main considerations in this respect are the internal mass transfer limitations, residence time distribution, heat management and pressure drop.

Internal mass transfer limitations can arise for relatively large particles. Reactants need to diffuse through the particle to reach the catalytically active sites, and for large particles this diffusion process may be so slow that it limits the observed reaction rate (Thiele, 1939).

In an ideal plug flow reactor, every molecule spends the same amount of time in the reactor. Real reactors, however,

* Corresponding author.
E-mail address:
m.v.sintannaland@tue.nl (M. van Sint Annaland).

https://doi.org/10.1016/j.cherd.2023.06.046

Nomenclature

Symbol Representation

A	Area [m^2].
Bi	Biot number [-].
c	Concentration [kg m^{-3}].
C_d	Drag coefficient [-].
C_p	Heat capacity [J kg^{-1} K^{-1}].
D_i	Diffusivity of species i [kg m^{-1} s^{-1}].
d	Diameter [m].
E	RTD function [-].
F	Flow fraction [-].
h	Enthalpy [J kg^{-1}].
h_v	Volumetric heat transfer coefficient [W m^{-3} K^{-1}].
h_W	Wall heat transfer coefficient [W m^{-2} K^{-1}].
K	Kinematic energy [J kg^{-1}].
L	Length [m].
M	Molar mass [kg mol^{-1}].
N	Number of data points [-].
Nu	Nusselt number [-].
P	Pressure [Pa].
Pe	P é clet number [-].
Pr	Prandtl number [-].
Q	Wall heat flux [W m^{-2}].
q	Thermal conduction term [W m^{-2}].
R	Gas constant [J K^{-1} mol^{-1}].
Re	Reynolds number [-].
s^3	RTD skewness [-].
T	Temperature [K].
t	time [s].
U	Superficial velocity [m s^{-1}].
$\mathbf{u}$	Velocity vector [m s^{-1}].
u_z	Axial velocity [m s^{-1}].
V	Volume [m^3].
x	Mole fraction [-].
Y_i	Mass fraction of species i [-].
z	Axial position [m].
α_{OV}	Overall heat transfer coefficient [W m^{-2} K^{-1}].
ΔP	Pressure drop [Pa].
ϵ	Porosity [-].
η	Viscosity [Pa s].
λ	Thermal conductivity [J m^{-1} K^{-1}].
ρ	Density [kg m^{-3}].
σ	RTD standard deviation [-].
τ	Stress tensor [Pa].
τ	Residence time [s].
Φ_v	Volumetric flow rate [m^3 s^{-1}].
Φ_m''	Superficial mass flux [kg m^{-2} s^{-1}].

Subscripts and superscripts Subscript Representation

B	Baffle.
e	Effective.
f	Fluid.
h	Hydraulic.
MC	Mixing cup.
m	Mean.
OV	Overall.
p	Particle.
r	Radial.
s	Solid.
*	Relative.

likely feature a residence time distribution due to preferential flow paths and dispersion phenomena. These phenomena are mostly governed by the particle size, whilst the former may also be the result of poor packing. A residence time distribution can influence the conversion and selectivity, and broaden the product distribution for complex reaction networks, as overall product yields depend on the residence time (Levenspiel and Bischoff, 1959).

The operating temperature governs the reaction rates, and consequently the conversion and product selectivity. To maintain this temperature, heat management is critical. Packed bed reactors are heated (or cooled) at the walls, and distribution of this heat along the transverse coordinate takes place through a combined process of solid conduction and fluid dispersion, which is governed by particle size and geometry (Lerou and Froment, 1977; Dixon and Cresswell, 1979). Especially for strongly endothermic or exothermic systems, reactor tubes of relatively low diameter are generally used to limit the impact of hot spots.

To achieve a low pressure drop, relatively large particles are required. However, the impact of pressure drop is slightly more nuanced. Whilst internal mass transfer limitations or hot spots may have severe consequences for the performance (in terms of conversion and selectivity or catalyst lifetime), the pressure drop of a reactor can mostly be seen as added process cost as long as it is lower than the operating pressure. Pressure drop needs to be compensated for by use of compressors, which increases the operating expenditures. Therefore, whilst low pressure drop is always strived for, the degree of pressure drop which is acceptable depends partially on the business case of a specific process.

These basic considerations exemplify the trade-offs in the design of randomly packed bed reactors. In industrial context, the large throughput of reactants necessitates the use of multi-tubular configurations with low diameter tubes for strongly endothermic or exothermic reactions to achieve sufficient heat exchange with the heat transfer fluid. Due to the random packing, it is difficult to achieve consistency amongst the tubes. This may manifest itself in maldistribution of the flow as the pressure drop over each tube varies (Shinnar et al., 1992). High consistency in packing, and a more lenient interplay between the three key operating parameters, may be provided by washcoated, structured reactor internals such as honeycomb monoliths or foams (Kapteijn and Moulijn, 2020; Heck et al., 2001; Twigg and Richardson, 2002). However, the low catalyst holdup limits the applicability of such structured internals for bulk chemical conversions (Vervloet et al., 2013).

The flexibility of Additive Manufacturing (AM), or 3D printing, of catalytic material may offer a bridge between the two classes; creating structured reactor internals with more lenient operating trade-offs and high catalyst holdup (Rosseau et al., 2022a). Whilst numerous additive manufacturing technologies are available to shape (mostly ceramic) catalyst material, the use of Direct Ink Writing (DIW) to produce logpile structures is the most mature and widely used in research context (Lawson et al., 2021). A DIW machine extrudes a viscous catalyst paste through a (circular) nozzle, laying down a pattern consisting of cylinders and stacking layers of these cylinders axially to create a 3D geometry. The porosity may be varied by varying the spacing between cylinders in every layer, and the orientation may be varied by offsetting every other layer whilst stacking (Lawson et al., 2020; Lefevere et al., 2018). Earlier experimental work

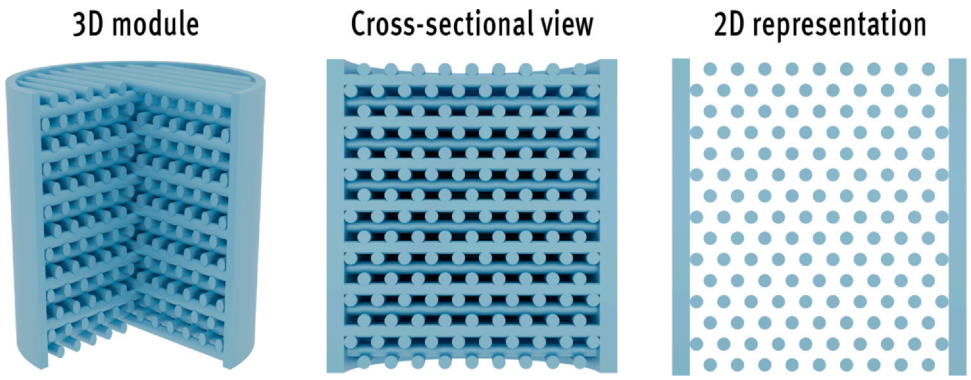

Fig. 1 – Visual depiction of the extraction of a 2D representation from a 3D logpile module. Shown is a staggered stacking configuration, where the intended flow direction is from bottom to top.

by our group has studied the transverse dispersion in these structures. This property is of specific interest since enhanced transverse dispersion facilitates radial heat transport. It was found that the transverse dispersion may be tailored by varying the geometry, but the magnitude of the transverse dispersion coefficients was rather low (Rosseau et al., 2022b). Given these conclusions, it is questioned whether these logpile structures can offer a degree of process intensification that can justify the use of the rather complex and expensive AM technology.

In the current work, the concept of baffled logpile structures will be used to design 3D printed structures that exploit the unique advantages of additive manufacturing to a higher degree. Specifically, it is envisioned that AM should be used for catalyst structures with customized properties and internal variations within the structures, as this is difficult to achieve with conventional methods. In a most basic consideration, baffles are flow-guiding elements. By providing significant flow resistance, or blocking the fluid flow entirely, fluid is forced to flow around these elements. Usually, the placement is perpendicular to the flow direction, converting axial convection into transverse convection (so-called cross-flow) and thereby enhancing the mixing of both mass and heat along the transverse coordinate (Li and Kottke, 1998; Berner et al., 1984; Yang and Hwang, 2003). This transverse convection provides enhanced contact of the fluid with the wall as it is forced against it, and this increases the wall-to-bed heat transfer significantly as the convective heat transfer rate exceeds the purely conductive rate which may dominate the near-wall heat transfer (Wehinger, 2022). The main downside of a baffle is the relatively high pressure drop that it generates. In addition to this, stagnant zones may appear which lead to underutilization of the reactor and a residence time distribution with a long tail (Phan and Harvey, 2010). By not using conventional, often inert, baffles, but 3D printing of catalytic baffles, the severity of these side effects may be mitigated. Specifically, porous baffles can be envisioned by densifying some parts of the logpile structure whilst leaving other sections more open. The increased resistance over the dense zone will guide the majority of the fluid around the baffle, but since it is still porous and part of the fluid may pass through the baffle, stagnant zones are avoided (Yang and Hwang, 2003). One of the main hypothesized benefits is the flexibility, as tuning of the porosity of the baffle should allow for different degrees of cross-flow, leveraging the fluid-phase heat transfer performance, residence time distribution and the pressure drop (Rosseau et al., 2022a). In this work, this trade-off will be studied in detail by assessing the hydrodynamic and wall-to-fluid heat transfer characteristics of different logpile designs with varying baffle parameters through OpenFOAM Computational Fluid Dynamics (CFD) simulations. The scope will be confined to 2D representations of baffled logpile geometries. Fig. 1 shows the extraction of such a 2D representation from a 3D logpile geometry. The main advantage of this representation is the significantly lower computational cost that is associated with 2D simulations compared to fully 3D simulations. This, in turn, allows for a broader range of geometries to be assessed, which is key for this exploratory work. In addition to this, the current scope is limited to fluid-phase heat transfer, as this is the main variable in the proof-of-concept of the cross-flow-generating structures. Solid-phase heat conduction is thus not taken into account, and it could be argued that its influence would be limited in the current setup, partially due to the relatively low thermal conductivity of commonly used catalyst materials. In addition to this, as is clear from Fig. 1, the 2D representation omits the logpile features which span the structures' diameter as these would block the flow entirely. Considering solid-phase heat conduction without these cylinders would severely underestimate the actual solid-phase heat transfer.

This paper is structured as follows. In the Methods section, the design variables of the structures under study are introduced and the simulation setup is described. This is followed by considerations on the performance metrics for the pressure drop, residence time distribution and heat transfer, used to evaluate the structures. In the Results section, the functioning of the baffle is first assessed, before going through some exemplary results in detail. This is followed by a full evaluation of all structures based on the performance metrics. The most promising structures are subjected to further investigations at varying superficial velocity in the final Results section, and these results are subsequently compared to the conventional packed bed of spheres. Finally, the impact of the 2D representation and the omission of the solid-phase heat transfer is discussed, followed by a conclusion.

2. Methods

2.1. *Geometries*

Five different structure classes are evaluated in this study; aligned, staggered, porous baffle, split-recombine and non-porous baffle. The different structure classes are visualized in Fig. 2 as a 2D representation where the white circles

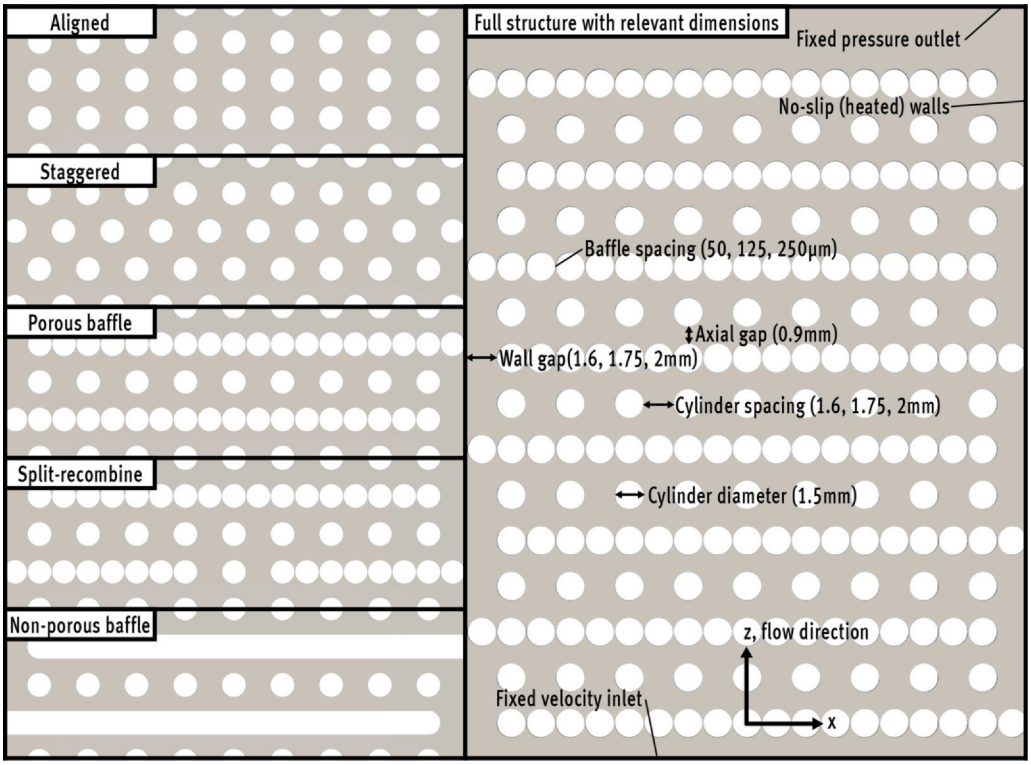

Fig. 2 – Axially repeating units of the different structure classes on the left and full porous baffle structure with relevant dimensions and boundary conditions on the right. Colored domain represents the fluid phase and white circles represent printed catalyst cylinders.

represent printed catalyst cylinders. The aligned and staggered structures are reference geometries as standard logpile structures (Lefevere et al., 2018). The porous baffle structure is a logpile structure designed as a conventional baffle with alternating attachment to opposite walls. The split-recombine design is similar to the porous baffle, but alternates centered baffle openings with baffle layers that are open on both sides at the wall, inspired by micromixers with a similar name (Habchi et al., 2019; Juraeva and Kang, 2020). The non-porous baffle is a reference structure, similar to the porous baffle design, but using a solid baffle block rather than a densified logpile zone. Every structure is based on an aligned grid of 15 by 9 cylinders of 1.5 mm diameter. The spacing between cylinders is either 1.6 mm, 1.75 mm or 2 mm, resulting in a structure diameter of approximately 3 cm. Assuming an axial stacking offset of 80%, which is common for structures made by DIW (Rosseau et al., 2022b), all structures have a height of 3.6 cm. These dimensions are also visualized in Fig. 2. The staggered structure has every odd axial layer offset by 50% in the transverse direction. For the baffled structures, additional cylinders are placed in certain gaps in the aligned structure at every odd layer. This is expressed as the relative baffle length (representing the length of the baffle as a percentage of the domain width, this definition introduces small variations as a function of baffle gap spacing). Following this section, structural variations will be expressed as three parameters: design, relative length and gap spacing of the baffle, to yield a total of 43 variations (all geometries and the resulting bed porosities are shown in the Appendix, in Table A.1.). The baffle gap spacing is the spacing of the gap between cylinders within the baffle (e.g. the aligned spacing minus the cylinder diameter), with a lower value of 50 μm in this work. This value was chosen in light of the limitations of DIW. Since this AM technology extrudes a viscous paste rather than solid cylinders, placement of objects close together will cause them to merge and this imposes a minimal distance. The reproducible 3D printing of such structures, especially in the context of the shrinkage that is often relevant for this technology, should be considered in further experimental work. Finally, it should also be noted that the cylinders are generated to be smooth. Printing of catalyst material may result in rough external surfaces, but considering both the proof-of-concept stage of the current work, as well as the relatively high uncertainty in roughness values, this is not considered (Buj-Corral et al., 2020; Hossain and Lu, 2023).

2.2. *Simulation setup and meshing*

The hydrodynamics and heat transfer properties were studied with the *OpenFOAM-v2106* software (OpenCFD Ltd.). *rhoReactingFoam* was selected as a solver, which is a transient solver for compressible, multicomponent flows with an optional chemical reaction module, based on the Pressure Implicit Method with splitting of operator for Pressure-Linked Equations (PIMPLE). The governing equations, describing the conservation of (species) mass, momentum and energy, are shown in Equations (1) to (4). In the current solver, the general Newtonian form of the stress tensor is used and the ideal gas law is used as an equation of state. The Sutherland equation describes the dependency of viscosity on temperature and the fluid thermal properties are assumed a polynomial function of temperature. In order to assess that the solver is working as expected, two relevant validation cases are documented in Appendix B.

$$\frac{\partial \rho}{\partial t} + \nabla \cdot (\rho \mathbf{u}) = 0 \tag{1}$$

$$\frac{\partial(\rho\mathbf{u})}{\partial t} + \nabla\cdot(\rho\mathbf{u}\mathbf{u}) = -\nabla p - \nabla\cdot\tau \tag{2}$$

$$\frac{\partial(\rho h)}{\partial t} + \nabla\cdot(\rho\mathbf{u}h) + \frac{\partial(\rho K)}{\partial t} + \nabla\cdot(\rho\mathbf{u}K) - \frac{\partial p}{\partial t} = -\nabla\cdot q \tag{3}$$

$$\frac{\partial(\rho Y_i)}{\partial t} + \nabla\cdot(\rho\mathbf{u}Y_i) = \nabla\cdot D_i\nabla Y_i \tag{4}$$

To study the performance of the novel geometries, two different cases were simulated; one transient simulation with tracer injection at constant temperature and one steady-state simulation with heated walls. The former was used to study the flow distribution within the structure, as well as the pressure drop and the residence time distribution. The latter was used to study the temperature profile within the structure and to obtain the volume-averaged wall-to-bed heat transfer coefficient.

These simulations were conducted with nitrogen as fluid at an inlet temperature of 300 K, a fixed outlet pressure of 1 atm and a superficial inlet velocity of 0.05 m s^{-1}. A no-slip velocity boundary condition was used for the structure and the reactor walls. The wall temperature was either set to a *zeroGradient* boundary condition (for tracer simulations) or a fixed value of 400 K (for simulations with heated walls). A *zeroGradient* temperature boundary condition was also imposed on the structure patch. In all transient simulations, the Courant number was employed to control the time step, with a maximum Courant number of 0.8.

The geometries were designed with the Blender software (Blender Online Community, 2022) and exported as stereolithography (.stl) file. The Blender .stl file was converted to an OpenFOAM mesh through the *blockMesh* and *snappyHexMesh* utilities. The former provides a 2D background mesh of square hexahedral cells and the latter removes the .stl geometry from the background mesh. *snappyHexMesh* provides various options for local refinement near the object that is placed in the background mesh. This allows for a detailed description of the boundary layers near the object, but also increases the number of cells significantly. In addition to this, to accurately describe the cylindrical features in the logpile structures under study, local refinement tends to introduce cells with a relatively high non-orthogonality which needs to be corrected for in the numerical schemes. Suitable parameters for the meshing procedure were determined through a grid size study with the pressure drop over a single baffle as response variable. The grid size of the background mesh was varied from 100 μm to 6.25 μm, local refinement was either used or not, and the surface-normal-gradient schemes either included a non-orthogonal corrector or not. The results can be expressed as the relative error and the relative (computational) cost, by comparing the result of a certain refinement to that of the finest refinement. The results of this grid size study are shown in Fig. 3.

As expected, the error decreases as a function of background refinement and as a function of local refinement. The latter is true solely for the cases with the non-orthogonal correction applied, as local refinement increases the average non-orthogonality from less than 2 degrees to over 15 degrees for all cases. Hence, it is implied that cases with local

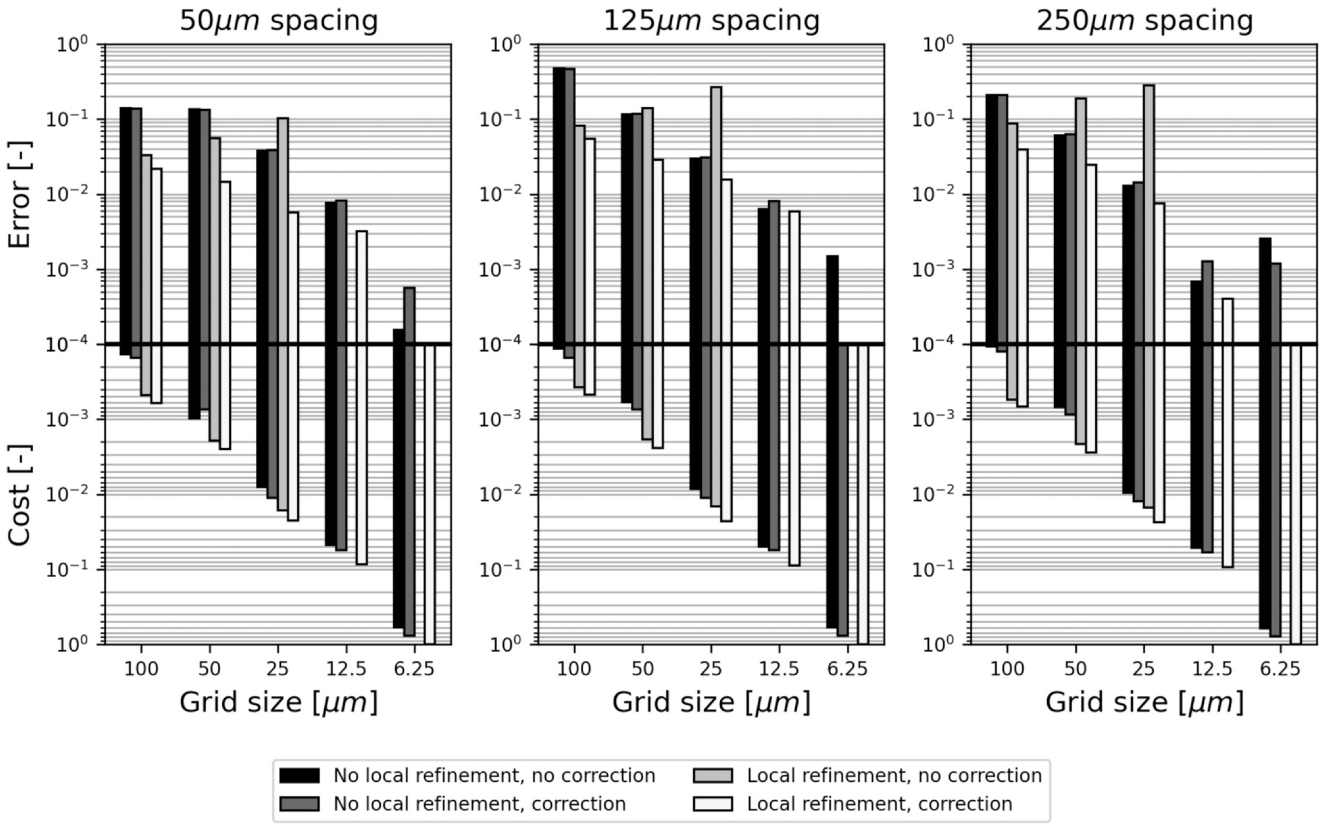

Fig. 3 – Grid size study as a function of *blockMesh* grid size, local refinement and non-orthogonal correction for the pressure drop over a single baffle. Error and cost are calculated relative to the case with a 6.25 μm background mesh with local refinement and the corrected surface-normal-gradient scheme. For the smallest two grid sizes with local refinement, the non-orthogonality was too high to yield a stable solution without applying the non-orthogonal corrector and hence, these results are not shown.

refinement require the non-orthogonal correction, whilst cases without local refinement yield an equal error regardless of the correction. Taking into account the average computational cost increase of 30% when using the non-orthogonal correction, cases without local refinement should be performed without the correction. For all baffle gap spacings, a background refinement of 25 μm yields acceptable errors at moderate computational cost. For the smallest two baffle gap spacings, local refinement is required to adequately describe the gap between cylinders and this will be used in all simulations. For a baffle gap spacing of 250 μm, local refinement is not strictly necessary to obtain a relative error similar to that of the other baffle gap spacings. For visual reference, the mesh obtained with these settings is visualised in the Appendix, as Fig. C.1.

All simulations were performed on the Dutch supercomputer. As an indication, performing the pressure drop and residence time simulation for 6 residence times for the porous baffle structure with 94.8% relative baffle length and 50 μm baffle gap spacing took 33 h and 9 min of wall clock time on 128 cores, equal to approximately 4234 core hours on AMD EPYC 7H12 CPU's. Performing the same simulation on a non-porous baffle structure (94.8% relative baffle length) took 15 h and 29 min of wall clock time on 128 cores, equal to approximately 1982 core hours. The latter was meshed without local refinement, yielding a total of 1175,060 cells and an average non-orthogonality of 0.91 degrees. This contrasts the former run with 2581,976 cells and an average non-orthogonality of 27 degrees, requiring the non-orthogonal correction, leading to the higher computational time.

Since the scope of the current work is on the hydrodynamics and the fluid-phase heat transfer induced by the various geometries, and the resulting influence on the operating trade-offs, the solid phase is not explicitly modelled. In addition to this, all simulations were conducted in 2D. Simulations of structures with three-dimensional baffles would increase the computational cost significantly, and with limited computational resources, this would not allow for the broad evaluation of structural parameters currently under study. As mentioned, considerations on the influence of the 2D nature of the simulations on the results are given in the Discussion section.

2.3. Performance metrics

2.3.1. Flow profiles

The flow profiles within the structure were sampled after simulating a time period corresponding to a single residence time without heated walls. The residence time is calculated through Equation (5), and ranges from 0.42 s (for the non-porous baffle with 94.8% relative baffle length) to 0.57 s (for the aligned structure with 250 μm baffle gap spacing) at an inlet velocity of 0.05 m s^{-1}. It was verified that a single residence time was sufficient to reach steady state for all structures, as this yielded a maximum relative error in the velocity field of less than 1% and a relative error in the pressure drop of less than 0.01%, approaching the significance of the grid size study. For qualitative assessment, the velocity field was visualized with the Paraview software (version 5.10), using the LIC (Line Integral Convolution) to represent the flow direction.

$$\tau = \frac{\epsilon V_{\text{domain}}}{UA_{in}} \tag{5}$$

The built-in OpenFOAM sampling tool was employed to extract the cell values of the axial component of the velocity vector over relevant transverse line segments. Specifically, the velocity through the wall gap and the baffle were sampled at every axial baffle layer. The velocities were multiplied by the respective cell areas, summed and averaged over the axial layers to yield the volumetric flow rate that passes next to the wall ($\Phi_{v,\text{wall}}$) and the flow rate that passes through the baffle ($\Phi_{v,\text{baffle}}$). From these values, the fraction of the flow that passes along the wall (F_W) and the fraction of the flow that is bypassing the baffled structure (F_B) are calculated according to Equations (6) and (7), respectively.

$$F_W = \frac{\Phi_{v,\text{wall}}}{\Phi_{v,in}} \tag{6}$$

$$F_B = \frac{\Phi_{v,\text{baffle}}}{\Phi_{v,in}} \tag{7}$$

2.3.2. Pressure drop

The pressure was sampled at the inlet and the outlet of a structure after one residence time has elapsed in the simulation. The built-in OpenFOAM sampling tool was used to extract cell values for the pressure along the transverse coordinate and these were area-averaged and subtracted to obtain the pressure difference. This pressure difference in 2D is not exactly representative for actual 3D printed structures, since the presence of additional supporting cylinders in the third dimension will provide more flow resistance and hence, results in increased pressure drop. However as mentioned, the computational cost for full 3D modelling of the structures is too high for such an initial broad evaluation, and the 2D values can be used for comparison between the different 2D cases. Further attention to the influence of this will be given in the Discussion section.

2.3.3. Residence time distribution

After one residence time has elapsed and the system is at steady state, a box of tracer of 1 mm high, spanning the transverse length, was placed at the inlet. The tracer has the same physical properties as nitrogen. After this, the simulation was continued for another five residence times. During this time, the outlet concentration profile was periodically sampled and the mixing cup concentration was calculated (Equation (8)) and stored. The evolution of the mixing cup concentration over time can be used to construct an E-curve via Equation (9). The E-curve, by definition of this equation, describes the residence time distribution as the normalized tracer concentration. The shape of such a curve, and particularly the location of the peak and length of the tail, can be used to characterize the performance of a chemical reactor (Rodrigues, 2021). For convenient relative comparison, the dimensionless time (t^*) is employed, as defined in Equation (10). To quantitatively compare residence time behavior, some statistics are calculated from the moments of the distribution, namely the mean residence time, the standard deviation and the skewness, as shown in Equations (11), (12) and (13), respectively (Fogler, 2014). It was found that 1000 sampling intervals provided adequate resolution to construct a representative E-curve.

$$c_{MC} = \frac{\sum x_{\text{tracer}} \frac{MP}{RT} u_z A_{\text{cell}}}{\sum u_z A_{\text{cell}}} \tag{8}$$

$$E(t^*) = \frac{c_{MC}(t^*)}{\int c_{MC}(t^*)dt^*} \tag{9}$$

$$t^* \equiv \frac{t}{\tau} \tag{10}$$

$$t_m = \int t^* E(t^*)dt^* \tag{11}$$

$$\sigma^2 = \int (t^* - t_m)^2 E(t^*)dt^* \tag{12}$$

$$s^3 = \sigma^{-\frac{3}{2}} \int (t^* - t_m)^3 E(t^*)dt^* \tag{13}$$

2.3.4. Heat transfer

The heat transfer performance is assessed through a steady state simulation with a constant wall temperature of 400 K. To determine the (local) volumetric heat transfer coefficient, the domain is divided into 100 segments over the axial coordinate. For each segment, the average wall heat flux and the mixing cup average temperature are combined to calculate the local volumetric heat transfer coefficient via Equation (14). The former is determined using the dedicated OpenFOAM functionObject and the latter is calculated via Equation (15). The calculated value can either be used on its own to visualize the heat transfer performance as a function of axial position, or averaged to obtain an overall volumetric heat transfer coefficient for a specific structure (Equation (16)).

In this study, the volumetric heat transfer coefficient will be used for comparison between different structures rather than the more conventional α_{OV}, defined in Equation (17). This was done since the width of the domain changes slightly as a function of the baffle gap spacing. The volumetric heat transfer coefficient compensates for these variations and therefore allows for a more fair comparison.

$$h_{v,\text{local}} = \frac{2}{d_{\text{domain}}} \frac{Q}{T_{MC} - T_{\text{wall}}} \tag{14}$$

$$T_{MC} = \frac{\sum T u_z A_{\text{cell}}}{\sum u_z A_{\text{cell}}} \tag{15}$$

$$h_v = \frac{1}{N} \sum h_{v,\text{local}} \tag{16}$$

$$\alpha_{OV} = \frac{1}{N} \sum \frac{Q}{T_{MC} - T_{\text{wall}}} \tag{17}$$

2.3.5. Dependence on velocity and comparison to packed bed of spheres

The most promising structures will be tested at different superficial velocities to explore the heat transfer–pressure drop trade-off as a function of the Reynolds number and compare this dependency to that of a packed bed of monodisperse spheres. Specifically, the superficial velocity will be varied from 0.05 m s^{-1} to 0.25 m s^{-1} in increments of 0.05 m s^{-1}.

For 2D chromatographic pillar arrays, structures similar to those currently under study, Vanapalli et al. (2007) achieved a good description of the pressure drop dependency using Equation (18), with C and m as fitted parameters. These authors used the hydraulic Reynolds number (Equation (19)) for fitting rather than the more conventional particle Reynolds number (Equation (20)). The required hydraulic diameter (d_h) can be determined via Equation (21).

$$\frac{\Delta P}{L} = \frac{\rho}{2}\left(\frac{U^2}{d}\right)_{\text{characteristic}} \frac{C}{Re^m_{\text{characteristic}}} \tag{18}$$

$$Re_h = \frac{\rho_f U d_h}{\epsilon \eta_f} \tag{19}$$

$$Re_p = \frac{\rho_f U d_p}{\eta_f} \tag{20}$$

$$d_h = \frac{\epsilon V_{\text{domain}}}{A_{\text{wetted}}} \tag{21}$$

The heat transfer performance is commonly captured in the Nusselt number, which can be fitted through the general form in Equation (22), with A, B and n as fitted parameters. Such a correlation generally includes a dependence on the Prandtl number, but since the current simulations are conducted for a single fluid (with only slight variations in Prandtl number as a function of temperature), this cannot be fitted and is lumped into the parameters A and B.

$$Nu_{OV} = \frac{\alpha_{OV} d_{\text{characteristic}}}{\lambda_f} = A + B Re^n_{\text{characteristic}} \tag{22}$$

For both the pressure drop and the Nusselt number, fitting of the dataset will be done using the *curve_fit* tool of Scipy (version 1.9.0) in Python 3.8.4. The quality of fitting will be assessed by calculating the Mean Average Percentage Error (MAPE), as defined in Equation (23) (for Nu_{OV}).

$$MAPE = \frac{1}{N} \sum \left| \frac{Nu_{OV} - \overline{Nu_{OV}}}{Nu_{OV}} \right| \tag{23}$$

The pressure drop in a packed bed of spheres is commonly expressed through the Ergun equation, Equation (24).

$$\frac{\Delta P}{L} = 150 \frac{\eta_f}{d_p^2} \frac{(1-\epsilon)^2}{\epsilon^3} U + 1.75 \frac{\rho_f}{d_p} \frac{1-\epsilon}{\epsilon^3} U^2 \tag{24}$$

Correlations for the heat transfer in a packed bed of spheres are more disputed, with a large spread in reported data, especially at lower Reynolds numbers (Li and Finlayson, 1977). The general expression for the overall heat transfer coefficient, including a transport resistance of the bed and a resistance provided by the wall-to-bed heat transfer, is shown in Equation (25) (with the definition of the Biot number as in Equation (26)) (Dixon, 1996). To be able to compare the current results with the heat transfer performance in a packed bed of spheres, the solid phase heat transfer contributions will be neglected, and this greatly simplifies the expressions for the effective radial thermal conductivity and the apparent wall heat transfer coefficient. The equations used are taken from the extensive work by Dixon and Cresswell (1979), and shown in Equations (27) and (28). The value of $Pe_{f,r}(\infty)$ is set to a value of 10 (Dixon, 2012).

$$\frac{1}{\alpha_{OV}} = \frac{1}{h_W} + \frac{d_{\text{domain}}}{6\lambda_{e,r}} \frac{Bi + 3}{Bi + 4} \tag{25}$$

$$Bi = \frac{h_W d_{\text{domain}}}{2\lambda_{e,r}} \tag{26}$$

$$\frac{1}{Pe_{e,r}} = \frac{1}{Pe_{f,r}} = \frac{\lambda_{f,r}}{\Phi''_m d_p C_{p,f}} = \frac{1}{Pe_{f,r}(\infty)} + \frac{\frac{2}{3}\epsilon}{RePr} \tag{27}$$

$$Nu_W = Nu_{W,f} = \frac{h_W d_p}{\lambda_f} = 0.6 Pr^{1/3} Re^{1/2} \tag{28}$$

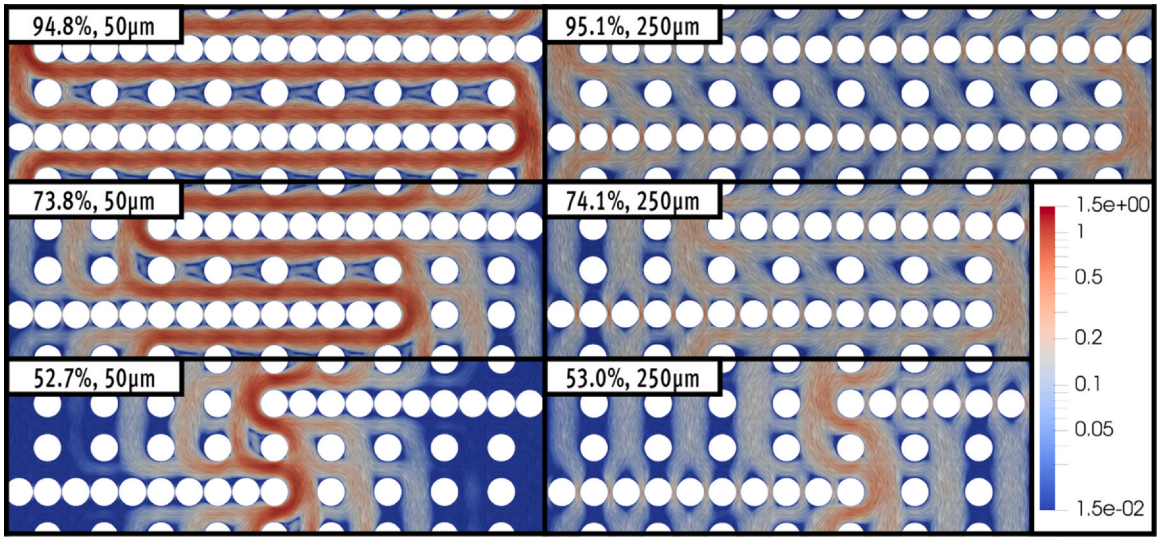

Fig. 4 – Flow profiles in six exemplary porous baffle structures of varying relative baffle length and gap spacing. Shown is the velocity magnitude (in m s^{-1}) on a log scale, with LIC representation to indicate the flow direction.

3. Results

3.1. *Flow profiles*

In Fig. 4, the hydrodynamics of several porous baffle structures are visualized to obtain a qualitative understanding of the influence of the different design variables on the degree of cross-flow. A similar visualisation for split-recombine structures is available as Fig. D.1 in the Appendix.

Whether the flow follows the imposed structure depends on the relative resistances of the different flow paths. Comparing the geometries with a baffle gap spacing of 250 μm to those with a baffle gap spacing of 50 μm, it is seen that a large fraction of the flow is bypassing through the structure, simply because the larger gaps provide a lower flow resistance. The spacing of the gaps is therefore critical in ensuring that the majority of the flow follows the imposed structure. It is also qualitatively seen that the relative baffle length influences the degree of bypassing, albeit to a lesser degree. The main observation regarding baffle length, however, is that shorter baffles lead to preferred flow through the center of the structure rather than along the walls. It can be expected that this limits the heat transfer performance as conduction through the stagnant near-wall fluid region is required, which is slow compared to convection-driven heat transfer.

Quantitative substantiation of these observations is given in Fig. 5. It can be seen that in general, split-recombine baffle designs exceed the degree of cross-flow of regular porous baffled structures, since the path length that the cross-flowing fluid needs to travel is only half as long. This, in turn, leads to a lower resistance along the imposed path and thus a larger fraction of the flow following it. Regardless of structure class, as expected, the baffle gap spacing is the key determining factor in ensuring that the flow follows the imposed structure, with a minor, linear-like, contribution of the relative baffle length. The most salient observation in this figure is in the graph on the right-hand side, where a

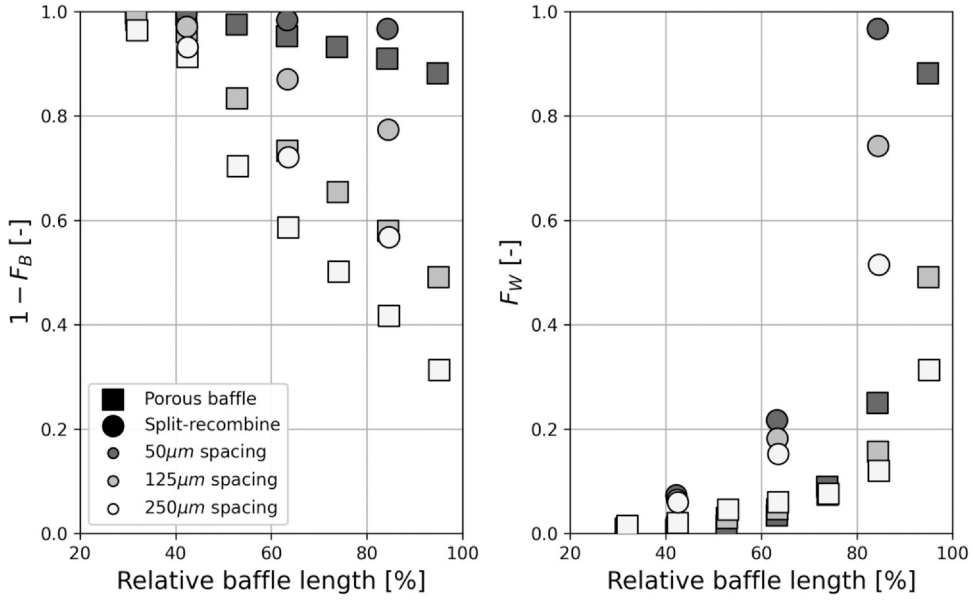

Fig. 5 – Fraction of the flow around the baffle ($1 - F_B$, left plot) and through the wall-gap (F_W, right plot) as a function of structure class, spacing and relative baffle length.

sharp decay in wall flow is seen as a function of relative baffle length. As wall flow is key in improved wall-to-bed heat transfer, this data strongly suggests that optimal geometries require the highest relative baffle length possible. Concluding these observations, it can be stated that the gap space governs *how well the baffle works* and that the relative baffle length determines *whether the baffle increases the fluid-wall contact*.

3.2. *E-curves and heat transfer*

Visualisation and sampling of the flow profiles yields an understanding of the interplay between the geometrical parameters and the degree of cross-flow. In this section, exemplary structures will be evaluated in detail to link the observed cross-flow behavior to the performance of the structure. Specifically, the residence time distribution and the distribution of heat throughout the structure will be assessed. Such an evaluation is necessary to provide the context for a comparison between the structures solely based on the performance parameters.

In Fig. 6, the E-curves of several structures are plotted in five graphs of three structural variations each. Snapshots of the tracer concentration are available in the Appendix as Figs. E.1, E.2 and E.3. The first graph of Fig. 6 contains the E-curves of an aligned, a staggered and a non-porous baffle structure, as reference cases. It is seen that all three structures exhibit a Gaussian-like E-curve with low skewness (s^3 = 0.04, 0.06 and 0.05, respectively). The aligned structure exhibits a slightly higher spread (σ = 0.18 compared to 0.15 for the staggered case), as the channels offer preferential flow paths and small stagnant volumes exist in the axial gaps

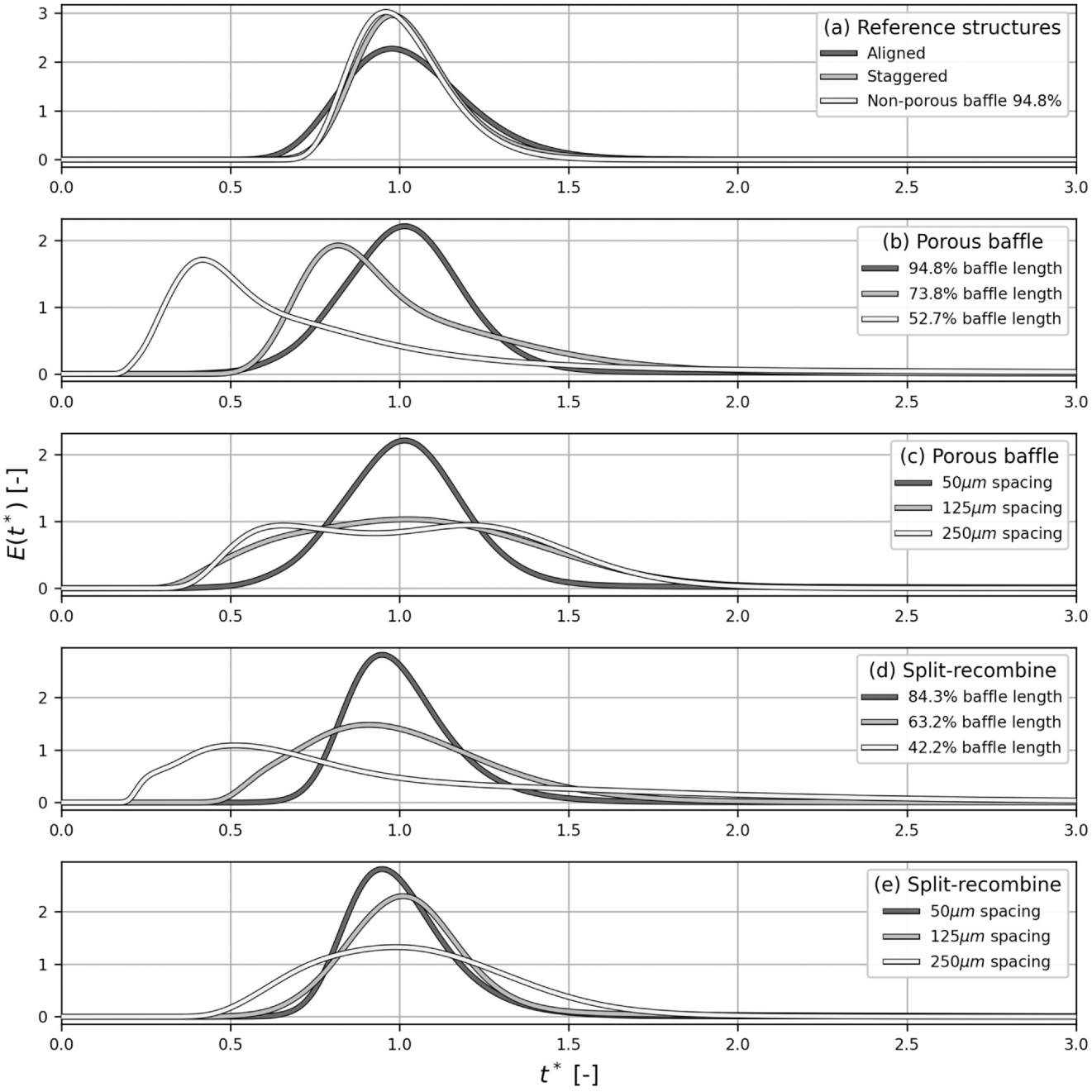

Fig. 6 – E-curves of several exemplary structures. Unless stated differently, the geometries with a baffle gap spacing of 50 μm and the highest relative baffle length are displayed. All simulations were executed until $t^* = 5$, but only the first 3 residence times are shown.

between cylinders. Regarding the non-porous baffled structure, it was stated in the Introduction that the pockets of stagnant volume in the wake of the baffles are a disadvantage of these structures. However, this is not observed in the E-curve or the corresponding tracer visualisation in Fig. E.1. Likely, the axial spacing of baffles in current design is too small to reach a significant stagnant volume and hence this effect is not observed. In the literature, conventional baffles are axially placed with spacing in the order of (tens of) centimeters, at least an order-of-magnitude larger than the current design (Yang and Hwang, 2003; Li and Kottke, 1998; Kizilaslan et al., 2018).

The second and fourth graph show variations of the relative baffle length for porous baffle and split-recombine structures, respectively. For both structures, the highest relative baffle length offers a relatively low standard deviation ($\sigma = 0.40$ and 0.32, respectively) and a low degree of tailing. Despite this, the calculated skewness is rather high with values of 1.20 and 1.21 respectively. This is due to the difference in slope on either side of the peak, the fact that the mean is not located at the peak and the normalization of the skewness by the (low) standard deviation. As the relative baffle length decreases, the peak moves more to the left, indicated flow bypassing through the center, and the tail increases as some tracer gets trapped in stagnant volume. This can be observed in the corresponding tracer profiles in Figs. E.2 and E.3. Despite the tailing, the skewness values are in the same order-of-magnitude as for the highest relative baffle length. This illustrates the skewness as a more general measure of the peak symmetry rather than a dedicated metric of the degree of tailing. Despite this, the combination of these two moments of the distribution gives an adequate representation of flow character of the structure. In the fourth graph, the split-recombine structure with 42.2% relative baffle length exhibits a slightly more complex curve, as the low baffle length in this design gives rise to two preferential flow paths rather than a single center flow (as visualized in Fig. E.3 in the Appendix). In addition to this, it can be observed that the peak of the porous baffle structure with 94.8% relative baffle length is located on the right-hand side of $t^* = 1$. This can be explained by flow short-circuiting, likely through the baffle openings near the wall (Fogler, 2014; Rodrigues, 2021; Bérard et al., 2020).

The third and fifth graph show variations in baffle gap spacing. Larger spacings lead to broadening of the peak and eventually to the emergence of two separate peaks, as seen in the curve for the porous baffle structure with 250 μm spacing. As the spacing increases, the resistance for fluid travelling through the baffle is decreased, leading to a significant fraction of the flow through the baffle. This fraction travels more slowly than the fluid bypassing through the larger gaps near the wall, and this leads to the observed peak separation. Again, the severity of peak broadening is less for the split-recombine case compared to the porous baffle. Since the imposed flow path is shorter and offers less resistance, there is less tendency for the fluid to bypass in the split-recombine structure.

In similar fashion, it is insightful to have a detailed look at the heat transfer behavior of the different structures before moving on to a direct comparison. This data is provided in Fig. 7, where the local heat transfer coefficient is plotted over the relative axial position (defined as $z^* \equiv \frac{z}{L}$). To support this analysis, snapshots of the temperature distribution and corresponding flow profiles in exemplary structures are available in the Appendix, as Fig. F.1. The reference curves in the first graph of Fig. 7 show that the heat transfer in the aligned and staggered structure is relatively low as the fluid is not actively forced against the walls and heat transfer occurs mostly through conduction. The h_v curve of the staggered structure shows a periodic pattern, which is the result of the fluid flowing closer to the wall at every other axial layer. A more exaggerated form of this periodicity is displayed by the non-porous baffle structure, as the heat transfer is enhanced at every baffle opening where fluid is forced against the wall, to decrease again in the more open transverse channels.

The curves of the porous baffle structure are similar to those of the non-porous structure, with a clear periodicity. As expected, the structure with 50 μm baffle gap spacing and 94.8% relative baffle length has slightly lower h_v values compared to its non-porous counterpart as not all of the fluid is forced against the wall and some passes through the baffles. The values decrease rapidly as a function of relative baffle length, which was already expected from the flow profiles in Fig. 4, as shorter baffles lead to relatively large zones of stagnant fluid near the wall. As a function of baffle gap spacing, the decrease is less pronounced.

The curves of the split-recombine structures also feature a periodic pattern, but the frequency is twice as low. This is a result of the center gap of the structure, forcing the cross-flowing fluid against the wall only once every four axial layers (on both sides) rather than every two axial layers (on a single side) as in the porous baffle structure. Another difference between the two structure classes is the larger amplitude of the curves for the split-recombine variant. It was shown in Fig. 5 that the flow follows the imposed structure very well for this structure class, meaning that almost all of the fluid is forced through the center gap rather than bypassing through the baffle, near the wall. This limits the heat exchange in this axial layer, with h_v values approaching zero. The influence of varying relative baffle length and baffle gap spacing seems less pronounced than for the porous baffle structure. This observation is also supported by Fig. 5, as both the wall flow fraction and the baffle flow fraction are higher for split-recombine structures compared to porous baffle structures.

From all curves in Fig. 7, it can be concluded that high relative baffle lengths are key to ensure adequate wall flow and the resulting heat transfer, with the baffle gap spacing being a more appropriate tuning parameter. The trade-off between these parameters and the pressure drop will be elaborated upon in the next section.

3.3. *Evaluation of structures*

In Table 1, the performance parameters of all structures are tabulated. For visual insights, the trade-off between heat transfer and pressure drop is shown in Fig. 8. These data generally confirm the hypotheses based on the flow profiles, E-curves and heat profiles of the previous sections. Some significant observations can be made.

Firstly, the baffled logpile structures provide a more flexible trade-off between pressure drop, RTD and heat transfer performance compared to the conventional logpile structures, as changing the design of the baffled structures leads to variations of the performance parameters within at least an order-of-magnitude. In contrast, the aligned and staggered structure classes only have the gap spacing as a

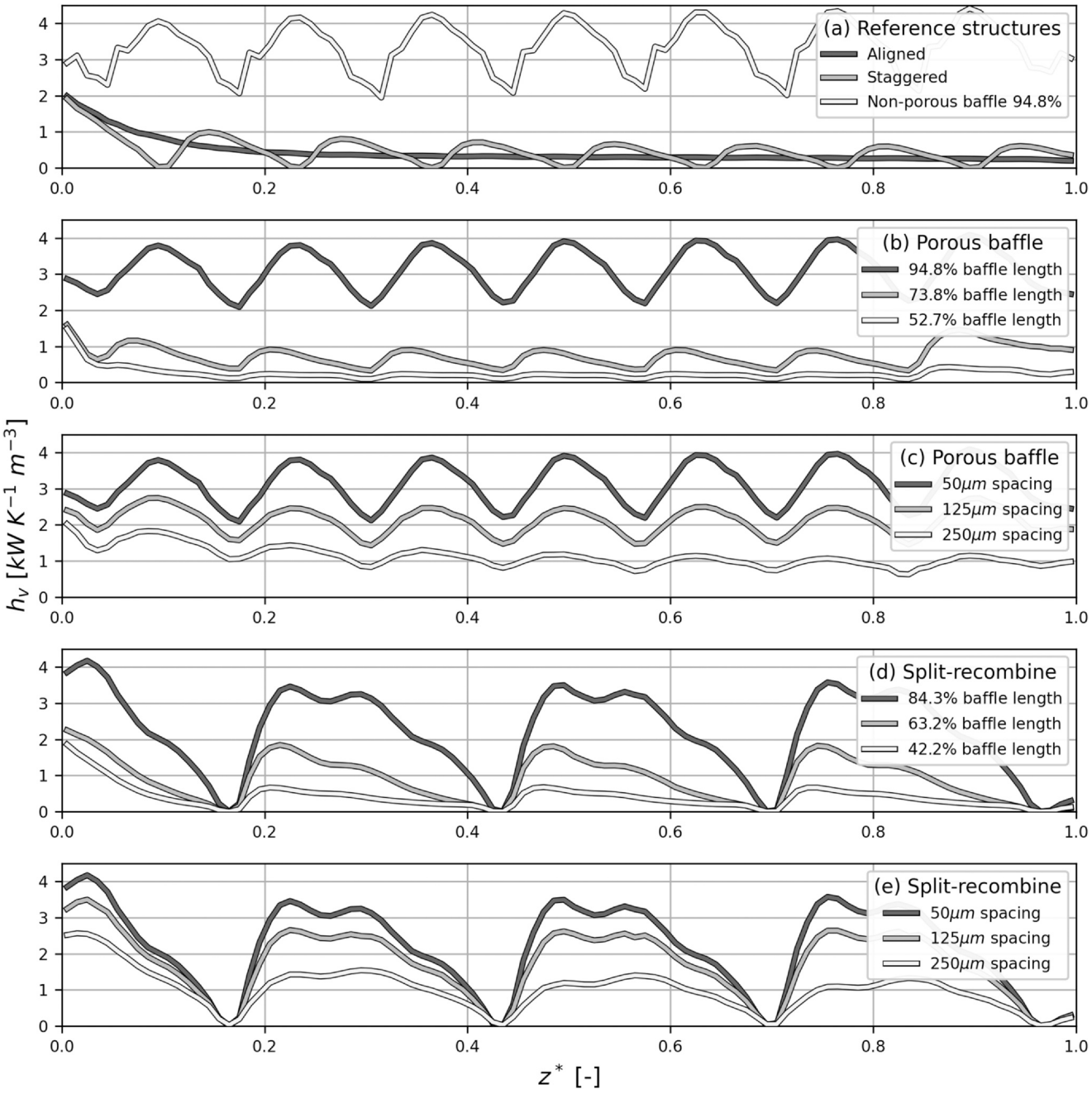

Fig. 7 – Local volumetric heat transfer coefficient as a function of relative axial position for several exemplary structures. Unless stated differently, the geometries with a spacing of 50 μm and the highest relative baffle length are displayed.

tunable parameter, and it is shown that this provides marginal variations in pressure drop, heat transfer and RTD parameters.

Secondly, both baffled logpile structures have favorable operating characteristics compared to the non-porous baffle structure. The porous baffle structure with the highest relative baffle length and the smallest spacing is able to provide 93.1% of the heat transfer at only 72.9% of the pressure drop compared to its non-porous baffle counterpart. The split-recombine structure with these parameters is able to provide 65.9% of the heat transfer at merely 18.0% of the pressure drop.

Thirdly, as expected, the highest relative baffle length is required to enable good heat transfer, and a favorable trade-off in all cases. In Fig. 8 it is observed that the marker size, indicating the pressure drop, and h_v values are strongly correlated, which is to be expected. Quantitatively, however, the heat transfer decreases much faster than pressure drop as a function of relative baffle length. Comparing the porous baffle structures of 95% relative baffle length to those of 84% relative baffle length shows that the h_v value decreases by a relative factor of 3.48 (250 μm spacing), 3.16 (125 μm spacing) and 1.88 (50 μm spacing) compared to the pressure drop. In contrast, this factor is 1.67 for the non-porous baffle structure, indicating that the comparison for baffled logpile structures is most favorable at the highest relative baffle length. Aside from the pressure drop and heat transfer, it is seen that structures with lower relative baffle lengths generally exhibit more skewed E-curves, which deviate largely from ideal plug flow behavior.

Finally, the split-recombine structure class is superior to the more conventional porous baffle design. In all instances, the pressure drop required to achieve a certain h_v value is lower for the split-recombine structures compared to the

Table 1 – Evaluation of the performance parameters for all structures under study. The pressure drop, ΔP is given in Pa, the volumetric heat transfer coefficient h_v is given in kW K^{-1} m^{-3} and the RTD parameters, σ and s^3, are dimensionless. All reported relative baffle lengths are averaged values, as actual values vary slightly as a function of baffle gap spacing.

Structure	250 μm spacing				125 μm spacing				50 μm spacing			
	ΔP	h_v	σ	s^3	ΔP	h_v	σ	s^3	ΔP	h_v	σ	s^3
Porous baffle 95%	3.83	1.12	0.36	0.08	11.56	2.11	0.38	0.18	23.66	3.11	0.40	1.20
Porous baffle 84%	3.28	0.56	0.35	0.17	9.50	0.92	0.31	0.39	18.17	1.75	0.37	1.28
Porous baffle 74%	2.82	0.40	0.29	0.12	7.75	0.45	0.34	0.46	13.76	0.75	0.44	1.04
Porous baffle 63%	2.37	0.34	0.28	0.15	5.87	0.31	0.57	0.74	9.34	0.40	0.68	1.40
Porous baffle 53%	1.73	0.28	0.53	0.25	3.54	0.23	0.96	1.67	4.87	0.25	0.80	1.86
Porous baffle 42%	0.62	0.18	1.04	2.19	0.87	0.18	0.82	2.03	1.03	0.19	0.79	1.97
Porous baffle 32%	0.33	0.18	0.79	2.02	0.43	0.19	0.75	1.99	0.50	0.21	0.76	1.98
Split-recombine 84%	2.46	1.02	0.30	0.12	4.64	1.75	0.36	0.93	5.85	2.20	0.32	1.21
Split-recombine 63%	1.64	0.43	0.30	0.25	2.66	0.68	0.45	0.93	3.08	0.89	0.36	0.77
Split-recombine 42%	0.51	0.28	0.87	1.38	0.67	0.34	0.81	1.29	0.78	0.40	0.72	1.01
Aligned	0.13	0.40	0.19	0.05	0.16	0.43	0.19	0.04	0.19	0.46	0.18	0.04
Staggered	0.22	0.43	0.17	0.09	0.26	0.47	0.16	0.07	0.30	0.50	0.15	0.06
Non-porous baffle 95%									32.46	3.34	0.14	0.05
Non-porous baffle 84%									24.54	1.98	0.16	0.07
Non-porous baffle 74%									18.01	0.86	0.32	0.24
Non-porous baffle 63%									11.66	0.42	0.65	1.31
Non-porous baffle 53%									5.52	0.25	0.74	1.78
Non-porous baffle 42%									1.06	0.19	0.75	1.93
Non-porous baffle 32%									0.51	0.21	0.73	1.96

porous baffle structures. The success of this geometry can be attributed to two factors: i) there is contact with the wall on both sides of the structure, enhancing heat transfer, and ii) the cross-flowing fluid needs to travel only from the wall to the center rather than the whole structure width, decreasing the pressure drop. Despite the superiority of the split-recombine structure, the highest heat transfer values are still reached by the porous baffle structures. Hence, these may be of interest to certain applications, despite the higher pressure drop penalty.

Taking these considerations into account, the following investigations will be conducted for six structures; the three structures with the highest relative baffle length and varying baffle gap spacing of both baffled logpile structure classes.

3.4. *Dependence on velocity and comparison to packed bed of spheres*

The pressure drop is plotted as a function of the particle Reynolds number in Fig. 9 for the six structures under study. The general trends expected from the data in Table 1 are still present, and no curve intercepts another curve, meaning that the relative values are independent of the Reynolds number. Also shown in Fig. 9 are the fitted curves based on Equation (18) with the cylinder diameter and superficial velocity as characteristic length and velocity, respectively. The fitted coefficients are shown in Table 2, and it can be seen that relatively low MAPE values are achieved for all structures. It can thus be concluded that the fitted equations

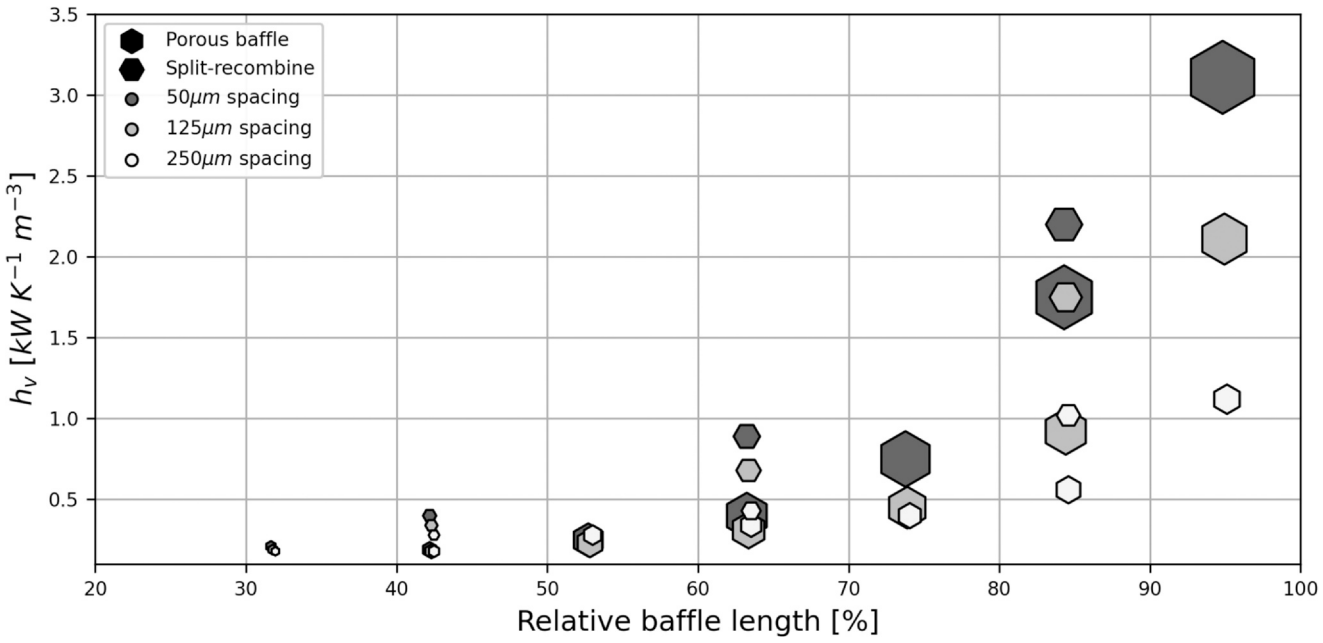

Fig. 8 – Volumetric heat transfer coefficient as a function of structure class, baffle gap spacing and relative baffle length. The area of the markers is proportional to the pressure drop to illustrate the h_v–ΔP trade-off.

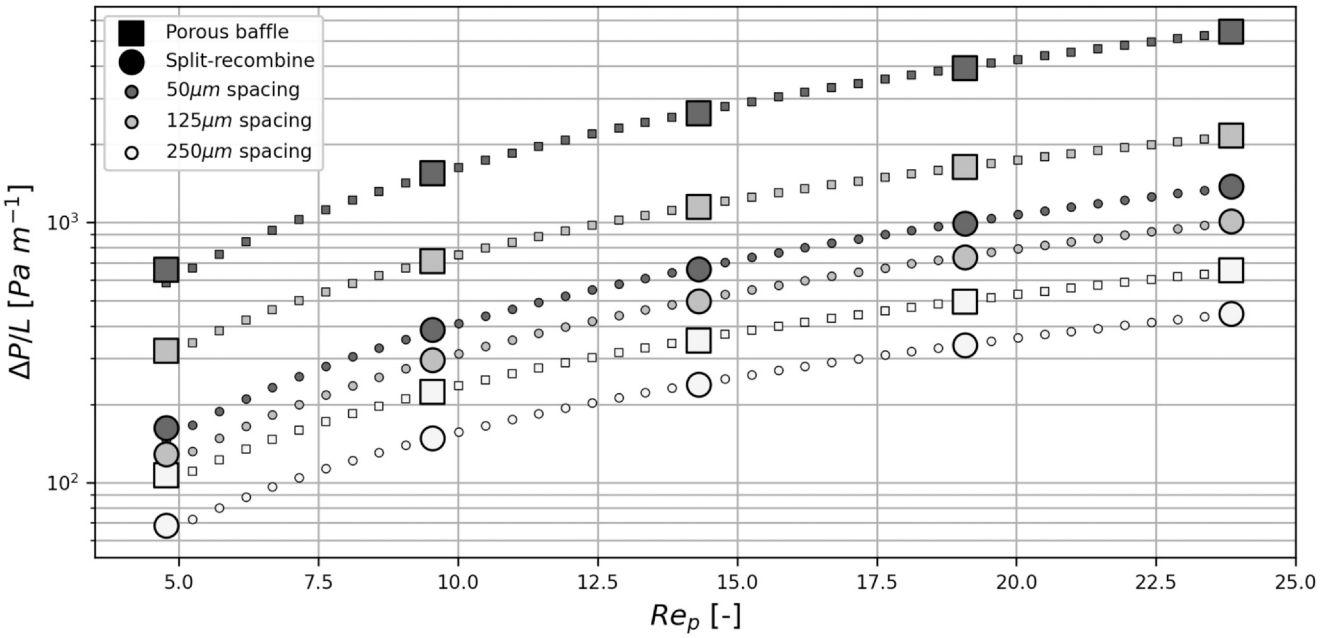

Fig. 9 – Pressure drop per reactor length as a function of the particle Reynolds number for six structures with the highest relative baffle length. Fitted correlations based on Equation (18) with the parameters in Table 2 are shown as dotted lines.

Table 2 – Fitted coefficients based on Equations (18) and (22) for pressure drop and Nusselt number, respectively. Parameter *n* in the correlation of the Nusselt number was fixed at 0.5.

Structure	C	m	MAPE	A	B	MAPE
Porous baffle 94.8%, 250 μm spacing	383	0.83	2.11%	0.50	0.22	0.29%
Porous baffle 94.9%, 125 μm spacing	1113	0.79	1.17%	1.34	0.16	0.42%
Porous baffle 95.1%, 50 μm spacing	1639	0.62	3.07%	1.49	0.39	1.16%
Split-recombine 84.3%, 250 μm spacing	236	0.80	1.64%	0.52	0.18	0.47%
Split-recombine 84.4%, 125 μm spacing	343	0.66	2.77%	1.01	0.19	0.51%
Split-recombine 84.6%, 50 μm spacing	395	0.61	2.96%	0.97	0.30	0.73%

provide a representative description of the pressure drop dependency. Following the work of Vanapalli et al. (2007), fitting was also attempted based on the hydraulic Reynolds number, but this did not yield lower MAPE values nor a more defined trend in C and *m* across the different structures. Hence, it was decided to use the more conventional definition of the Reynolds number. Whilst it is tempting to attempt to fit the pressure drop as a global function for all six structures (using geometrical properties such as the porosity and baffle gap spacing in C and *m*), such a description simplifies the underlying physical phenomena too greatly since unique structures with defined properties are being studied. Some simplification was attempted by setting the value of *m* as a constant at either 0.5 or 1 (the latter value representing a purely linear relation between pressure drop and superficial velocity), but this increased the MAPE fourfold on average and was thus abandoned. Vanapalli et al. (2007) also observed that various geometries could not be captured in a single correlation. From a qualitative point of view, it is observed that the value of *m* decreases as the baffle gap spacing decreases, thus increasing the order of the superficial velocity in this equation. This is likely due to the locally higher interstitial velocities in structures of lower baffle gap spacing.

In Fig. 10, the overall Nusselt number is shown as a function of the particle Reynolds number alongside fitted lines based on Equation (22), with fitted coefficients shown in Table 2. It was noticed that fitting with only two parameters and *n* fixed at 0.5 (a common value for laminar heat transfer (Bird et al., 2006)), yields low MAPE values and this was adopted. Comparable to the pressure drop data, fitting with the hydraulic diameter as characteristic length did not provide an improved description of the trends and therefore the more conventional particle Reynolds number is used. Again, the relative trends between structures are in line with the expectations from Table 1. However, the fitted parameter *B* has a relatively low value, indicating poor scaling of the heat transfer performance as a function of the Reynolds number. This can be explained by a larger degree of bypassing as the velocity increases. Ideally, the flow fraction around the baffle should be constant as the velocity is increased, but this is not observed, as shown in Fig. G.1 in the Appendix. Increasing the velocity shifts the relative resistances within the structure and this leads to a larger degree of bypassing. This effect is less obvious from the RTD characteristics of these simulations, tabulated in the Appendix, as Table H.1. The most significant trend in this data is a decrease in skewness as a function of Re_p, especially for smaller baffle gap spacings, but it was already concluded that the relationship between this

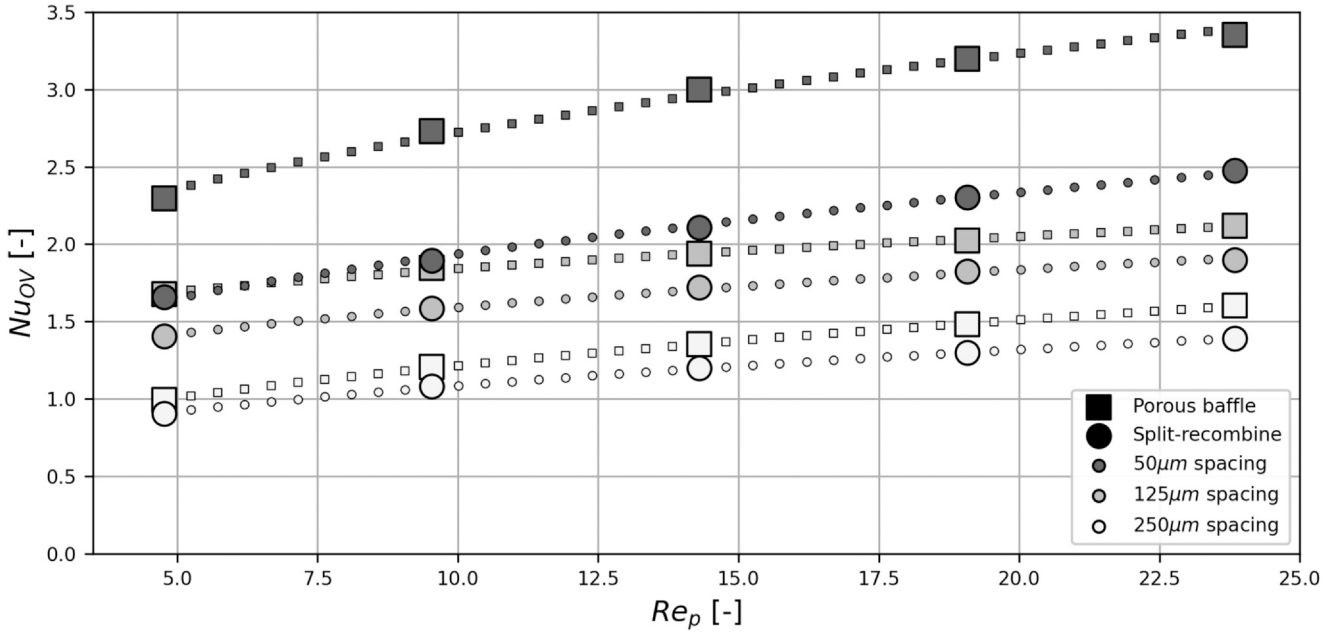

Fig. 10 – Overall Nusselt number as a function of the particle Reynolds number for six structures with the highest relative baffle length. Fitted correlations based on Equation (22) with the parameters in Table 2 are shown as dotted lines.

parameter and reactor performance is difficult to interpret. As for the standard deviation, the values appear to be relatively constant (especially compared to the differences present in Table 1). As with all observed effects thus far, the split-recombine structures suffer less from this phenomenon compared to the porous baffle structures.

To compare the performance of the six optimal structures to that of a packed bed of monodisperse spheres, the Nusselt number is plotted against the pressure drop in Fig. 11. It is clearly seen that the pressure drop required to achieve a certain heat transfer rate is far lower in the baffled logpile structures compared to the packed bed. A shortcoming of this analysis is the constant reactor length rather than constant catalyst volume, since a packed bed of spheres has a higher catalyst holdup. However, such a correction would decrease both the Nusselt number and pressure drop equally and the general trend is thus the same.

4. Discussion

The scope of this work was explicitly limited to 2D simulations without a solid-phase heat transfer contribution. Both of these assumptions enable lower computational cost and the large amount of structures currently under study, but the implications of these assumptions on the applicability of the current results require discussion. This mainly relates to the 2D nature of the simulations, which introduces some complexity in translating the results to reactor modules. This will first and foremost concern the pressure drop. In a 3D logpile representation, axial stacking layers spanning the width of the structure are present, and it can be expected that these increase the apparent pressure drop. To approximate the magnitude of this effect, a staggered structure was simulated both in 2D and in 3D. It was chosen to keep a constant interstitial velocity and thus scaling the superficial velocity as the porosity changes from 75.6% to 54.7% from the 2D to the 3D representation. The pressure drop approximately doubled in the 3D geometry compared to its 2D counterpart. Using this as a rough estimate of the 2D–3D scaling effect, the curves in Fig. 11 would shift quite significantly but the baffled logpile structures would still outperform the packed bed of spheres. A more delicate effect that results from the 3D stacking is an increase in tortuosity compared to fully 2D simulations. This likely increases the overall heat transfer rate thanks to the increased transverse dispersion. In turn, this effect could counteract the aforementioned shifting of the curves in Fig. 11. Such estimates require detailed attention in future research efforts, as the actual values depend largely on the implementation of the baffle designs in 3D modules. This is not trivial since the current representation is cubic, whilst chemical reactors are generally cylindrical. Orthogonal placement of baffles is likely suboptimal as wall contact is limited and tailored designs are required. The exact designs, and other structural variations such as the number of baffles per unit reactor length, are open research questions for future work.

The next point of discussion is related to the omission of the solid phase in the current simulations and the implications for heat transfer. To start, the correlations used for the packed bed of spheres are not necessarily valid in the limit of $\lambda_s = 0$, and quite some spread in estimates for Nu_{OV} was noticed amongst different literature correlations in this limit. Despite the spread and associated uncertainty, the relative position of the curve for the packed bed of spheres in Fig. 11 does not change. It could even be hypothesized that the inclusion of solid phase heat transfer will be beneficial for the baffled logpile structures since these feature cylinders spanning the reactor width. Transport of heat through such cylinders is likely faster than transport through a packed bed of spheres, which proceeds via point contacts between particles for solid-to-solid heat transfer. Finally, to approximate

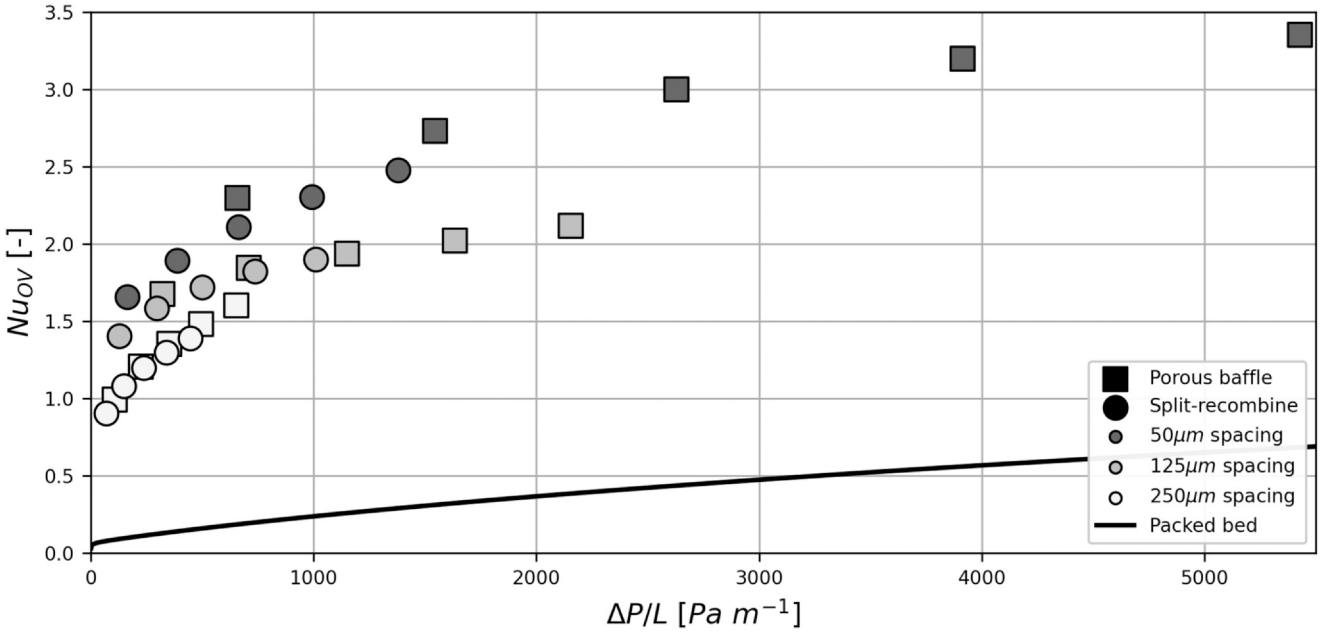

Fig. 11 – Overall Nusselt number as a function of the pressure drop for six structures with the highest relative baffle length alongside the trade-off for a packed bed of 1.5 mm spheres and 37% porosity.

the relevance of the omitted fluid-to-solid heat transfer in a packed bed of spheres, the Gunn correlation was used (Gunn, 1978). This yielded values for the associated Nusselt number of approximately an order-of-magnitude larger than the currently calculated Nu_{OV}. Thus at these operating conditions, the associated resistance is likely negligible. Using the Ranz-Marshall correlation for the fluid-to-solid heat transfer of an individual cylinder, which is likely more relevant in the context of the logpile structures, a Nusselt number in the same order-of-magnitude as Nu_{OV} was found (Bird et al., 2006). These arguments point out that solid phase heat transfer is likely to further improve the heat transfer performance of the baffled logpile structures, which should be assessed in future work.

Finally, it should be acknowledged that the studied velocities are relatively low. To discuss the practical applicability of such values, it is helpful to convert the used velocities to Gas Hourly Space Velocities (GHSV). At 0.05 m s^{-1}, the GHSV ranges from 12,500 to 20,000 h^{-1} (the variations are explained by the varying bed porosity of the different structures). In the final evaluation in Section 3.4, this is increased to approximately 75,000 h^{-1}. Such values are considered relatively high for the operation of catalytic fixed bed reactors at pilot scale (Guilera et al., 2020). Whilst further increasing of the velocity would be relevant to study the influence of turbulence on the operating characteristics, maintaining appropriate GHSV values at these conditions would require significantly larger structures. At the current stage of the DIW technology, it is not likely that such structures can be manufactured at the relevant scale.

5. Conclusions

The presented results demonstrate that baffled logpile structures can be used to provide process intensification in the design of packed bed reactors. It was found that the pressure drop required to achieve a certain heat transfer rate is significantly lower compared to non-porous baffled structures and packed beds of spheres, and that variations of baffle gap spacing may be used to tailor the trade-off to the requirements of a specific chemical process. To further develop this novel concept beyond the broad proof-of-concept stage, recommendations were given for more detailed simulations including the solid-phase heat transfer and 3D stacking variations.

Declaration of Competing Interest

The authors declare that they have no known competing financial interests or personal relationships that could have appeared to influence the work reported in this paper.

Acknowledgements

This article is based on research undertaken in relation to a project (ZEOCAT-3D) which has received funding from the European Union's Horizon 2020 research and innovation program, under Grant Agreement No. 814548. The authors would like to thank the EU Horizon 2020 program for this opportunity. This publication only reflects the author's views

and neither the funding Agency nor the European Commission are responsible for any use that may be made of the information contained therein. This work made use of the Dutch national e-infrastructure with the support of the SURF Cooperative using grant no. EINF-1478 and grant no. EINF-3116

Appendix A. Structural variations and bed porosities

Table A.1.

Table A.1 – Bed porosity (or gas holdup) of the various structures. All reported relative baffle lengths are averaged values, as actual values vary slightly as a function of baffle gap spacing.

Structure	250 μm spacing	125 μm spacing	50 μm spacing
Porous baffle 95%	69.6%	67.3%	65.7%
Porous baffle 84%	70.8%	68.5%	67.0%
Porous baffle 74%	72.0%	69.8%	68.4%
Porous baffle 63%	73.2%	71.1%	69.7%
Porous baffle 53%	74.3%	72.3%	71.0%
Porous baffle 42%	75.5%	73.6%	72.3%
Porous baffle 32%	76.7%	74.9%	73.7%
Split-recombine 84%	70.8%	68.5%	67.0%
Split-recombine 63%	73.2%	71.1%	69.7%
Split-recombine 42%	75.5%	73.6%	72.3%
Aligned	80.2%	78.7%	77.6%
Staggered	79.2%	77.6%	76.5%
Non-porous baffle 95%			58.2%
Non-porous baffle 84%			60.4%
Non-porous baffle 74%			62.6%
Non-porous baffle 63%			64.8%
Non-porous baffle 53%			66.9%
Non-porous baffle 42%			69.1%
Non-porous baffle 32%			71.3%

B. Solver validation

In this section, the *rhoReactingFoam* solver will be validated by comparing the calculated drag coefficient and heat transfer coefficient to correlations from the literature for flow around a single cylinder. Validation of the drag coefficient ensures that the solver adequately describes the flow resistance, which is related to the observed pressure drop. For this study, a case is simulated with nitrogen flow around a single cylinder of 1.5 mm diameter, centered in a 2D domain of 1 cm by 1 cm. Two meshes were generated (both with and without local refinement) with the settings as described in the Methods section. The built-in OpenFOAM *forceCoeffs* functionObject was used to extract the drag coefficient at five different superficial velocities (from 0.05 m s^{-1} to 0.25 m s^{-1} in increments of 0.05 m s^{-1}). The obtained values can be compared to Equation (B.1), which was proposed by Cheng (2013) to describe the relationship between the drag coefficient and particle Reynolds number for flow

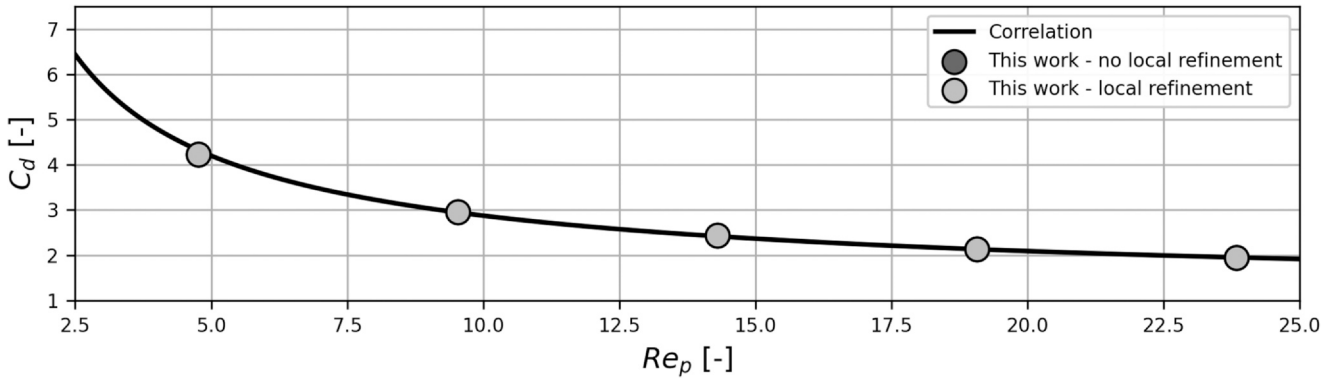

Fig. B.1 – Validation of the drag coefficient. Line represents the empirical correlation (Equation (B.1)) and markers represent simulation output with and without local refinement. Markers overlap completely.

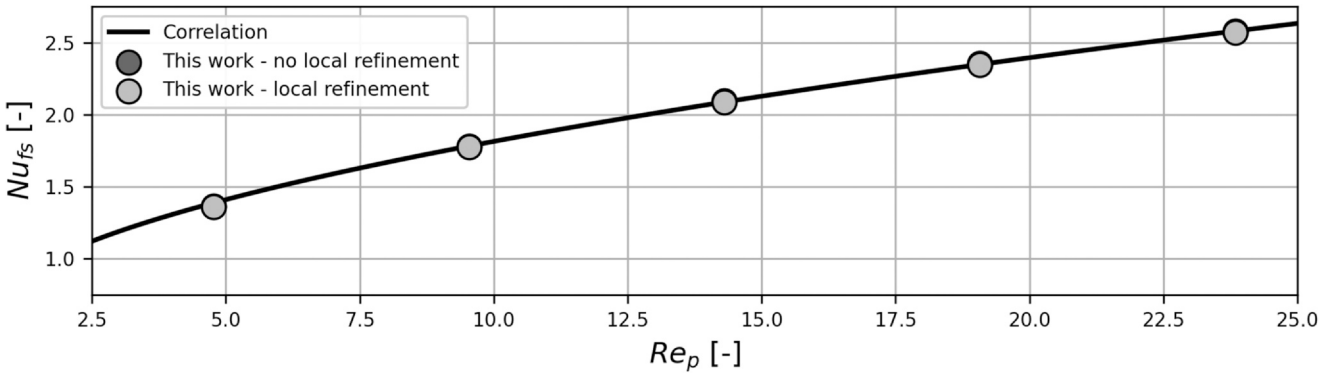

Fig. B.2 – Validation of the Nusselt number. Line represents the empirical correlation (Equation (B.2)) and markers represent simulation output with and without local refinement. Markers overlap completely.

around a single cylinder. This equation is based on empirical data and is valid for $0.2 < Re_p < 200000$. The comparison between this correlation and the values obtained from simulations is shown in Fig. B.1. A good agreement is observed, with MAPE values of 0.8% for both refinement levels. This is considered adequate, also taking into account the variability in available empirical data (Cheng, 2013; Tritton, 1959; Qu et al., 2013).

$$C_d = \frac{11}{Re_p^{0.75}} + 0.9\left(1 - \exp\left(-\frac{1000}{Re_p}\right)\right) + 1.2\left(1 - \exp\left(-\left(\frac{Re_p}{4500}\right)^{0.7}\right)\right) \tag{B.1}$$

The same case setup was used to validate the implementation of the heat transfer coefficient, the only exception being a fixed temperature imposed on the cylinder patch. The heat exchange between the cylinder (with a temperature of 400 K) and the fluid (with an inlet temperature of 300 K) was extracted with the built-in OpenFOAM *wallHeatFlux* functionObject, and this was converted to the associated Nusselt number following the method in Section 2.3.4. The obtained values can be compared to Equation (B.2), which is reported in Bird et al. (2006), where it is specifically mentioned that this correlation is appropriate for small Re_p. The comparison between this correlation and the values obtained from simulations is shown in Fig. B.2. Again, the observed agreement (with MAPE values of 0.5% and 0.6% for the simulations without and with local refinement, respectively) is considered adequate for validation of the solver.

$$Nu_{fs} = (0.376Re_p^{1/2} + 0.057Re_p^{2/3})Pr^{1/3} + 0.92\left(\ln\left(\frac{7.4055}{Re_p}\right) + 4.18Re_p\right)^{-1/3} Re_p^{1/3}Pr^{1/3} \tag{B.2}$$

C. Mesh refinement visualisation

Fig. C.1.

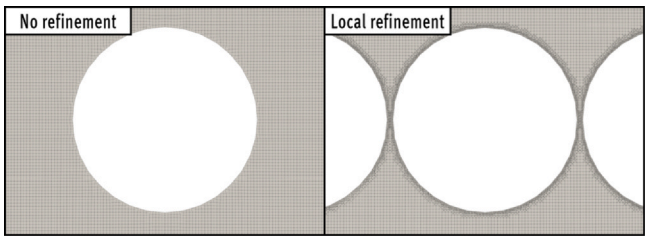

Fig. C.1 – Paraview visualisation of the mesh for a case without local refinement (left, an aligned structure) and a case with local refinement (right, a porous baffle structure with 50 μm spacing). Both were created with a background mesh refinement of 25 μm.

D. Split-recombine flow profiles

Fig. D.1.

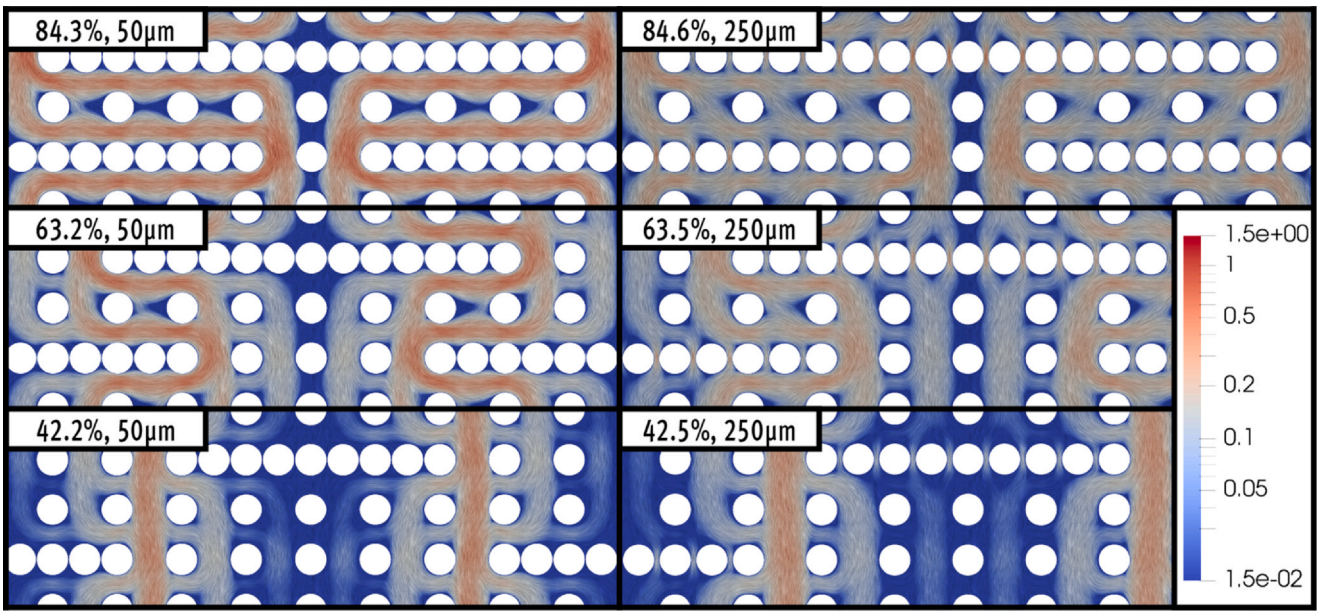

Fig. D.1 – Flow profiles in six exemplary split-recombine structures of varying relative baffle length and gap spacing. Shown is the velocity magnitude (in m s^{-1}) on a log scale, with LIC representation to indicate the flow direction.

E. RTD tracer visualisation

Figures E.1, E.2, E.3.

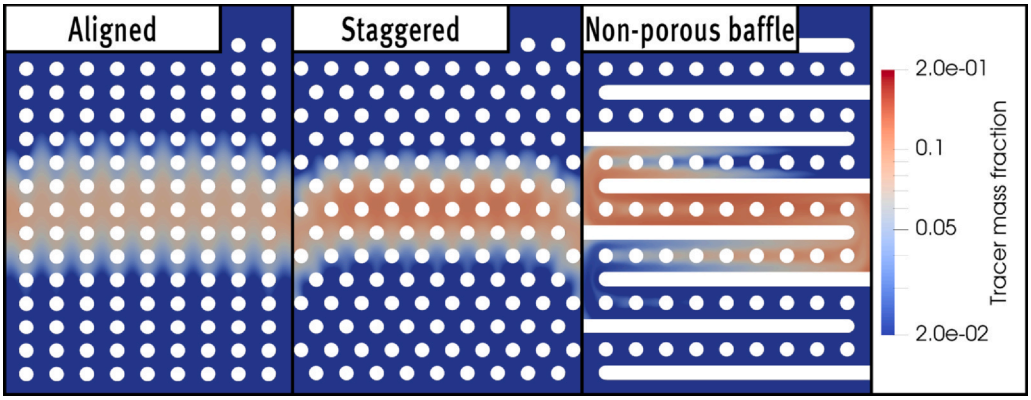

Fig. E.1 – Tracer profiles of three reference structures at $t/\tau = 0.5$. All three have a baffle gap spacing of 50 µm, corresponding to a cylinder gap of 1.6 mm. The tracer mass fraction is shown on a log scale.

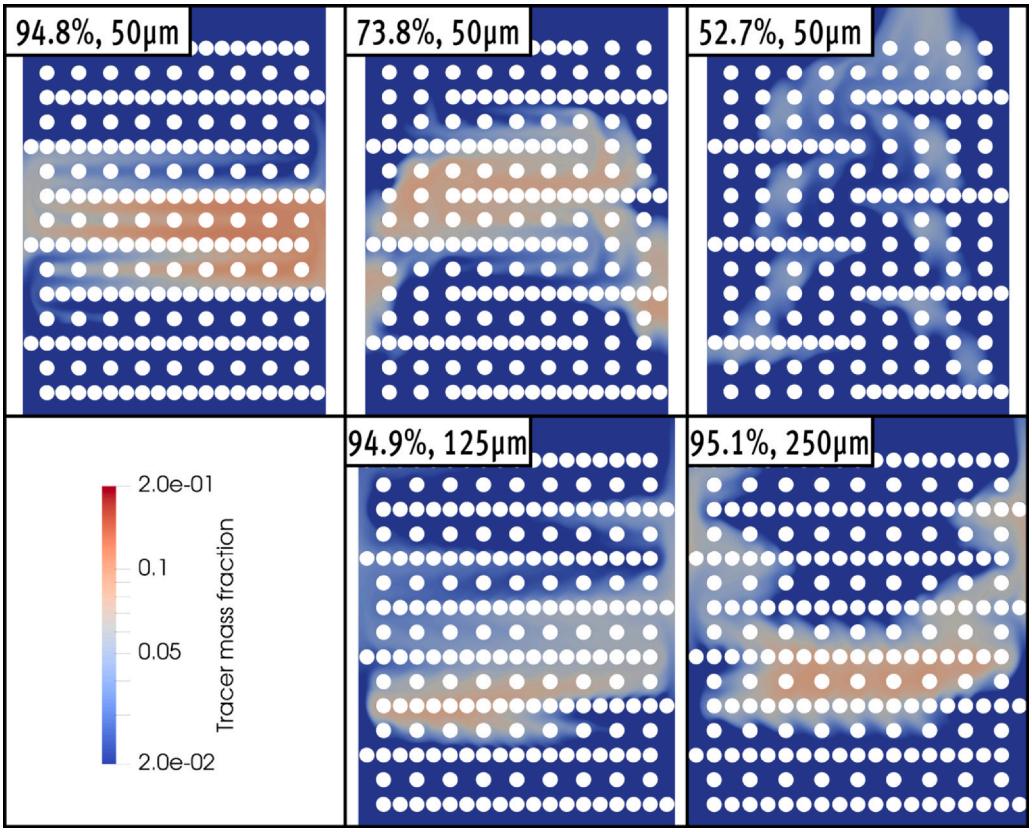

Fig. E.2 – Tracer profiles in five porous baffle structures at $t/\tau = 0.5$. The tracer mass fraction is shown on a log scale.

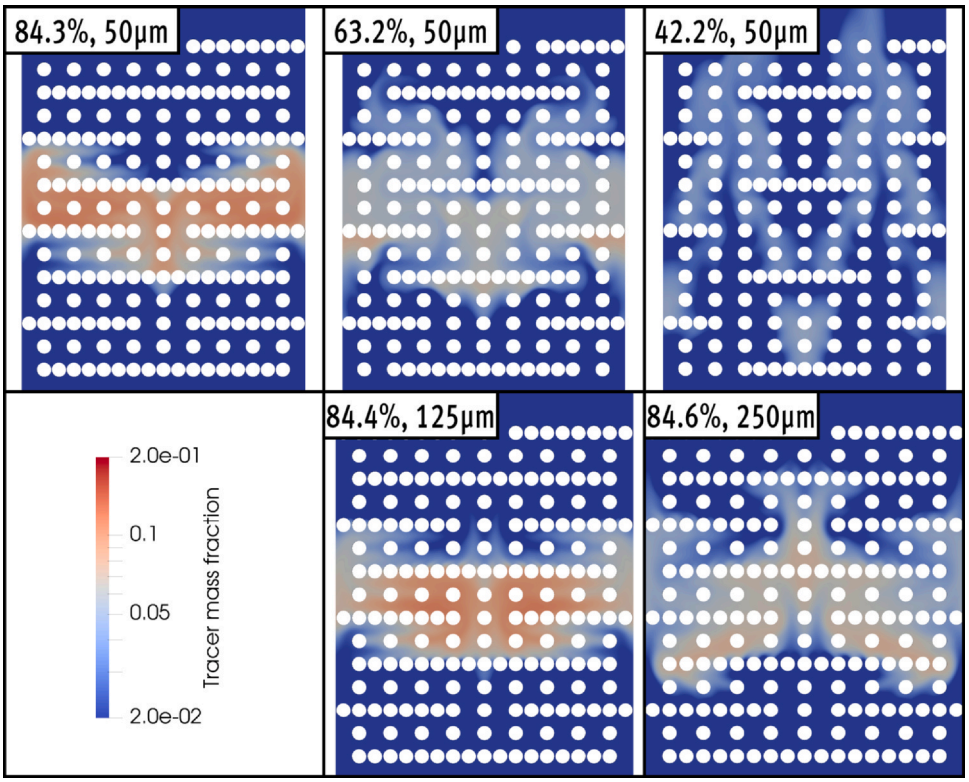

Fig. E.3 – Tracer profiles in five split-recombine structures at $t/\tau = 0.5$. The tracer mass fraction is shown on a log scale.

F. Temperature profiles

Fig. F.1.

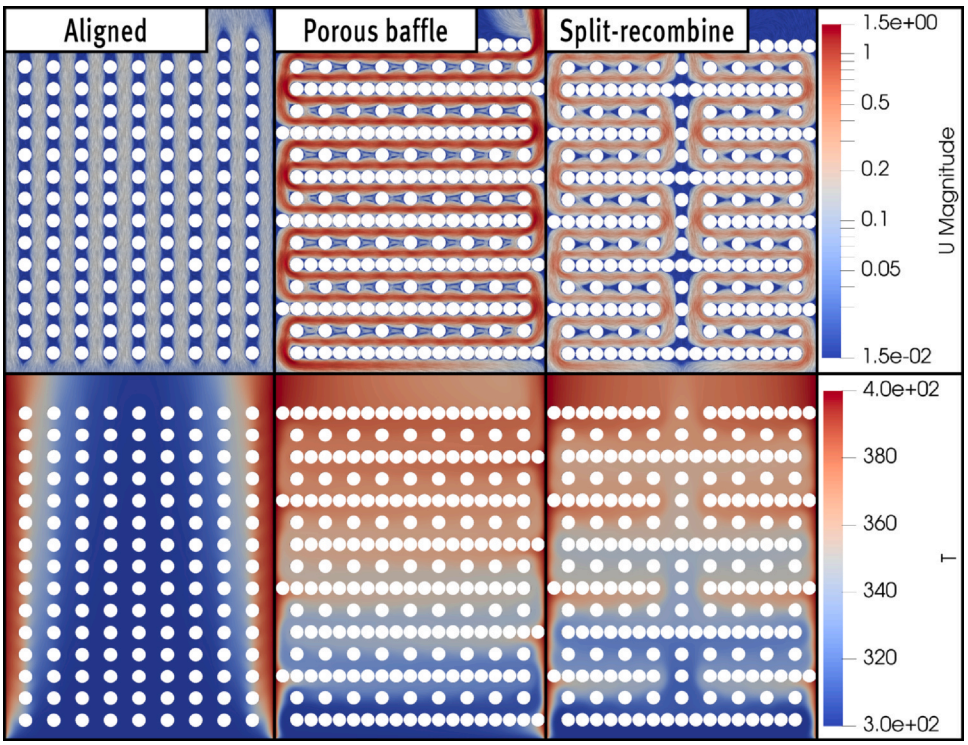

Fig. F.1 – Flow (top) and temperature (bottom) profiles of three exemplary structures of the smallest spacing and the highest relative baffle length. Shown in the top figure is the velocity magnitude (in m s^{-1}) on a log scale, with LIC representation to indicate the flow direction.

G. Flow fraction as a function of Reynolds number

Fig. G.1.

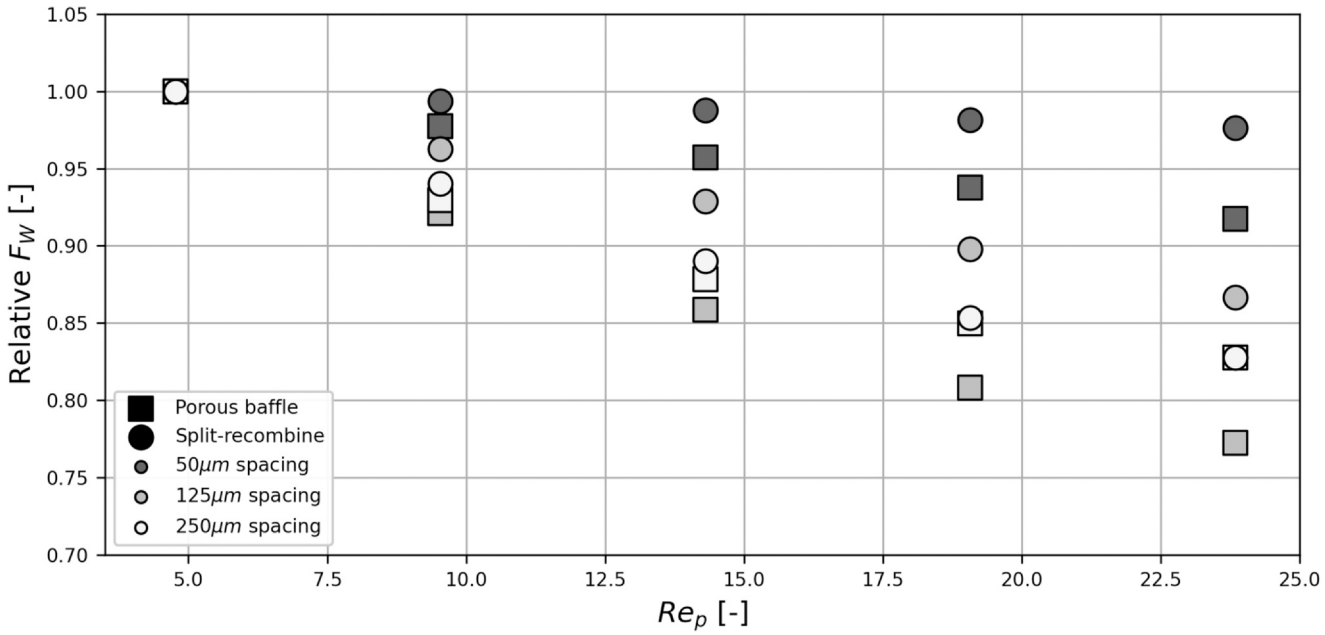

Fig. G.1 – Relative fraction of the flow through the wall-gap for the six optimal structures, as a function of Reynolds number.

H. RTD statistics as a function of the particle Reynolds number

Table H.1.

Table H.1 – Evaluation of the dimensionless RTD parameters as a function of the particle Reynolds number for two different structures. All reported relative baffle lengths are averaged values, as actual values vary slightly as a function of baffle gap spacing.

Structure	Re_p	250 μm spacing		125 μm spacing		50 μm spacing	
		σ	s^3	σ	s^3	σ	s^3
Porous baffle 95%	4.77	0.36	0.08	0.38	0.18	0.40	1.20
	9.54	0.35	0.01	0.42	0.13	0.35	0.79
	14.3	0.35	0.01	0.45	0.14	0.31	0.42
	19.1	0.36	0.05	0.48	0.15	0.30	0.27
	23.8	0.36	0.04	0.50	0.20	0.31	0.20
Split-recombine 84%	4.77	0.30	0.12	0.36	0.93	0.32	1.21
	9.54	0.32	0.10	0.29	0.58	0.30	0.85
	14.3	0.35	0.12	0.27	0.35	0.32	0.73
	19.1	0.38	0.15	0.27	0.24	0.35	0.67
	23.8	0.41	0.17	0.28	0.20	0.37	0.63

References

Afandizadeh, S., Foumeny, E.A., 2001. Design of packed bed reactors: Guides to catalyst shape, size, and loading selection. Appl. Therm. Eng. 21, 669–682.

Allen, K.G., vonBackström, T.W., Kröger, D.G., 2013. Packed bed pressure drop dependence on particle shape, size distribution, packing arrangement and roughness. Powder Technol. 246, 590–600.

Berner, C., Durst, F., McEligot, D.M., 1984. Flow around baffles. J. Heat. Transf. 106, 743–749.

Bird, R.B., Stewart, W.E., Lightfoot, E.N., 2006. Transport Phenomena, 2nd ed. Wiley, Hoboken, New Jersey.

Blender Online Community, 2022.Blender - a 3d modelling and rendering package.http://www.blender.org.

Buj-Corral, I., Domínguez-Fernández, A., Gómez-Gejo, A., 2020. Effect of printing parameters on dimensional error and surface roughness obtained in direct ink writing (diw) processes. Materials 13, 2157.

Bérard, A., Blais, B., Patience, G.S., 2020. Experimental methods in chemical engineering: Residence time distribution—rtd. Can. J. Chem. Eng. 98, 848–867.

Cheng, N.S., 2013. Calculation of drag coefficient for arrays of emergent circular cylinders with pseudofluid model. J. Hydraul. Eng. 139, 602–611.

Dixon, A.G., 1996. An improved equation for the overall heat transfer coefficient in packed beds. Chem. Eng. Process. - Process. Intensif. 35, 323–331.

Dixon, A.G., 2012. Fixed bed catalytic reactor modelling—the radial heat transfer problem. Can. J. Chem. Eng. 90, 507–527.

Dixon, A.G., Cresswell, D.L., 1979. Theoretical prediction of effective heat transfer parameters in packed beds. AIChE J. 25, 663–676.

Fogler, H.S., 2014. Elements of chemical reaction engineering, 4th ed. Pearson, Harlow.

Friend, C.M., Xu, B., 2017. Heterogeneous catalysis: a central science for a sustainable future. Acc. Chem. Res. 50, 517–521.

Guilera, J., Boeltken, T., Timm, F., Mallol, I., Alarcón, A., Andreu, T., 2020. Pushing the limits of sng process intensification: high ghsv operation at pilot scale.ACS Sustainable. Chem. Eng. 8, 8409–8418.

Gunn, D.J., 1978. Transfer of heat or mass to particles in fixed and fluidised beds. Int. J. Heat. Mass Transf. 21, 467–476.

Habchi, C., Ghanem, A., Lemenand, T., Valle, D.D., Peerhossaini, H., 2019. Mixing performance in split-and-recombine milli-static mixers—a numerical analysis. Chem. Eng. Res. Des. 142, 298–306.

Hagen, J., 2015. Catalyst Shapes and Production of Heterogeneous Catalysts. Industrial Catalysis. Wiley, Hoboken, New Jersey, Hoboken, pp. 211–238.

Heck, R.M., Gulati, S., Farrauto, R.J., 2001. The application of monoliths for gas phase catalytic reactions. Chem. Eng. J. 82, 149–156.

Hossain, S.S., Lu, K., 2023. Recent progress of alumina ceramics by direct ink writing: Ink design, printing and post-processing. Ceram. Int. 49, 10199–10212.

Juraeva, M., Kang, D.J., 2020. Mixing performance of a cross-channel split-and-recombine micro-mixer combined with mixing cell. Micromachines 11.

Kapteijn, F., Moulijn, J.A., 2020. Structured catalysts and reactors - perspectives for demanding applications. Catal. Today 383, 5–14.

Kizilaslan, M.A., Demirel, E., Aral, M.M., 2018. Effect of porous baffles on the energy performance of contact tanks in water treatment. Water 10, 1084.

Kraushaar-Czarnetzki, B., Müller, S.P., 2009. Shaping of Solid Catalysts. In: de Jong, K. (Ed.), Synthesis of Solid Catalysts. Wiley, Hoboken, New Jersey, pp. 173–199.

Lawson, S., Adebayo, B., Robinson, C., Al-Naddaf, Q., Rownaghi, A., Rezaei, F., 2020. The effects of cell density and intrinsic porosity on structural properties and adsorption kinetics in 3D-printed zeolite monoliths. Chem. Eng. Sci. 218, 115564.

Lawson, S., Li, X., Thakkar, H., Rownaghi, A.A., Rezaei, F., 2021. Recent advances in 3D printing of structured materials for adsorption and catalysis applications. Chem. Rev. 121, 6246–6291.

Lefevere, J., Mullens, S., Meynen, V., 2018. The impact of formulation and 3D-printing on the catalytic properties of ZSM-5 zeolite. Chem. Eng. J. 349, 260–268.

Lerou, J.J., Froment, G.F., 1977. Velocity, temperature and conversion profiles in fixed bed catalytic reactors. Chem. Eng. Sci. 32, 853–861.

Levenspiel, O., Bischoff, K.B., 1959. Backmixing in the design of chemical reactors. Ind. Eng. Chem. 51, 1431–1434.

Li, C.H., Finlayson, B.A., 1977. Heat transfer in packed beds-a re-evaluation. Chem. Eng. Sci. 32, 1055–1066.

Li, H., Kottke, V., 1998. Effect of baffle spacing on pressure drop and local heat transfer in shell-and-tube heat exchangers for staggered tube arrangement. Int. J. Heat. Mass Transf. 41, 1303–1311.

Mitchell, S., Michels, N.L., Pérez-Ramírez, J., 2013. From powder to technical body: The undervalued science of catalyst scale up. Chem. Soc. Rev. 42, 6094–6112.
Phan, A.N., Harvey, A., 2010. Development and evaluation of novel designs of continuous mesoscale oscillatory baffled reactors. Chem. Eng. J. 159, 212–219.
Qu, L., Norberg, C., Davidson, L., Peng, S.H., Wang, F., 2013. Quantitative numerical analysis of flow past a circular cylinder at reynolds number between 50 and 200. J. Fluids Struct. 39, 347–370.
Ravindran, K., Madhu, G., 2020. Impact of shape and size of catalysts on the physical properties and pressure drop in fixed bed catalytic systems. Int. J. Innov. Technol. Explor. Eng. 9, 1103–1109.
Rodrigues, A.E., 2021. Residence time distribution (rtd) revisited. Chem. Eng. Sci. 230, 116188.
Rosseau, L.R.S., Middelkoop, V., Willemsen, J.A.M., Roghair, I., van Sint Annaland, M., 2022a. Review on additive manufacturing of catalysts and sorbents and the potential for process intensification. Front. Chem. Eng. 4, 834547.
Rosseau, L.R.S., Schinkel, M.A.M.R., Roghair, I., van Sint Annaland, M., 2022b. Experimental quantification of gas dispersion in 3d-printed logpile structures using a noninvasive infrared transmission technique. ACS Eng. Au 2, 236–247.
Shinnar, R., Doyle, F.J., Budman, H.M., Morari, M., 1992. Design considerations for tubular reactors with highly exothermic reactions. AIChE J. 38, 1729–1743.
Thiele, E.W., 1939. Relation between catalytic activity and size of particle. Ind. Eng. Chem. 31, 916–920.
Tritton, D.J., 1959. Experiments on the flow past a circular cylinder at low reynolds numbers. J. Fluid Mech. 6, 547–567.
Twigg, M., Richardson, J., 2002. Theory and applications of ceramic foam catalysts. Chem. Eng. Res. Des. 80, 183–189.
Vanapalli, S., terBrake, H.J.M., Jansen, H.V., Burger, J.F., Holland, H.J., Veenstra, T.T., Elwenspoek, M.C., 2007. Pressure drop of laminar gas flows in a microchannel containing various pillar matrices. J. Micromech. Microeng. 17, 1381–1386.
Vervloet, D., Kapteijn, F., Nijenhuis, J., Van Ommen, J.R., 2013. Process intensification of tubular reactors: Considerations on catalyst hold-up of structured packings. Catal. Today 216, 111–116.
Wehinger, G.D., 2022. Improving the radial heat transport and heat distribution in catalytic gas-solid reactors. Chem. Eng. Process. - Process. Intensif. 177, 108996.
Yang, Y.T., Hwang, C.Z., 2003. Calculation of turbulent flow and heat transfer in a porous-baffled channel. Int. J. Heat. Mass Transf. 46, 771–780.